

Highlights

Fatigue growth modelling of three-dimensional cracks with the Extended Isogeometric Boundary Element Method

Matheus Rocha, Jon Trevelyan, Edson Denner Leonel

- the XIGABEM scheme is extended to crack propagation in 3D for the first time
- A novel algorithm is presented to propagate the crack in a way that guarantees the required inter-patch continuity
- The scheme is shown to reproduce reference solutions well using a small number of degrees of freedom

Fatigue growth modelling of three-dimensional cracks with the Extended Isogeometric Boundary Element Method

Matheus Rocha^{a,b}, Jon Trevelyan^b, Edson Denner Leonel^a

^a*Department of Structural Engineering, São Carlos School of Engineering, University of São Paulo, Av. Trabalhador São Carlense, 400, São Carlos, 13566-590, São Paulo, Brazil*

^b*Department of Engineering, Durham University, South Road, Durham, DH1 3LE, , United Kingdom*

Abstract

This paper proposes the fatigue crack growth modelling of three-dimensional geometries with the eXtended Isogeometric Boundary Element Method (XI-GABEM). The formulation combines the advantages of the dual Boundary Element Method (BEM), the isogeometric approach, and an enrichment strategy for surfaces containing the crack front. The dual BEM approach relies on a boundary-only mesh, eliminating a re-meshing task for internal cracks. The isogeometric approach applies NURBS basis functions to describe both geometry and mechanical fields, allowing accurate representation of curved shapes and improving convergence over classical polynomial functions. The enrichment strategy stems from the Williams expansion of displacements at the crack front, with parameters directly interpolating Stress Intensity Factors (SIFs), removing costly post-processing tasks. The hoop stress criterion and Schollmann criterion are used as crack growth criteria and are combined with a novel least squares strategy to define the updated crack front. Since this study addresses multi-patch discretisation of crack surfaces, additional strategies ensure continuity between patches as required by the enrichment field. Three numerical applications demonstrate the ability of the formulation to model fatigue in curved 3D geometries under various loading conditions, allowing a novel comparison between crack growth criteria.

Keywords: Extended isogeometric boundary element method, Enriched formulations, Three-dimensional fracture mechanics, Fatigue crack growth,

1. Introduction

The fatigue crack propagation phenomenon requires attention in the structural design phase of many mechanical components that are subjected to cyclical loading. In the high-cycle regime, engineers consider load amplitudes small enough not to cause an imminent collapse, but able to trigger a damage accumulation at regions containing intrinsic material flaws. As a result, these cracks propagate under operational loads, and engineers seek to ensure that cracks do not grow to a length that will result in material failure. In this context, the correct assessment of the required number of load cycles prior to failure is of major interest in ensuring structural safety.

The experimental observation of the high-cycle fatigue phenomenon reveals a relationship between the crack growth rate and the associated number of cycles. Specifically, the Paris-Erdogan Law uses concepts from Linear Elastic Fracture Mechanics (LEFM) to relate this rate to Stress Intensity Factors (SIFs). However, analysing complex three-dimensional components using classic analytical solutions is often impractical, as these solutions are only available for a limited set of cases. In this context, numerical methods have emerged as a suitable and powerful choice for fatigue modelling, given their robustness in the mechanical analysis of solids and structures.

Among the existing numerical methods, the Finite Element Method (FEM) is the standard option for both industrial and research applications and is also widely used for the fatigue analysis of three-dimensional components [1, 2, 3, 4]. However, the stress singularity at the crack front demands a fine mesh for accurate analysis. In addition, the crack growth process requires a re-meshing procedure for each propagation step. These two issues are responsible for increasing the FEM computational cost, which can cause large, industrially relevant problems to become intractable. Recently, alternative strategies have emerged for the fatigue assessment of solids, e.g. peridynamics [5, 6, 7, 8] and phase-field modelling [9, 10, 11, 12, 13]. While peridynamics presents an attractive approach in terms of capturing dynamic effects such as crack branching, it fails to capture some of the important physics, for example the propagation speed of an elastic wave. For the phase-field modelling, the bottleneck is the need for a fine mesh to accurately compute the phase variables, which can result in computationally demanding analyses.

Another successful numerical technique for the fatigue life assessment is the eXtended/Generalised FEM (X/GFEM). In this approach, the approximation of the mechanical fields incorporates additional functions based on the known solution space for the specific problem under study. These new functions are introduced as enrichment terms, and their selection improves convergence order and eliminates the need for re-meshing in crack growth analyses. The seminal work of Sukumar et al. [14] applies the X/GFEM to three-dimensional fatigue crack propagation, and it has been followed by several other studies [15, 16, 17, 18, 19, 20, 21]. These works demonstrate the accuracy and robustness that the proper choice of enrichment functions brings to the FEM, but they also introduce concerns as they may lead to an ill-conditioned algebraic system.

In three-dimensional analysis of engineering components, CAD representations are the standard tool for their geometrical modelling, particularly when complex geometries are involved. In this sense, the Isogeometric approach (IgA), first proposed by Hughes et al. [22], is an attractive strategy to simplify the numerical modelling task. In IgA, both the geometry and mechanical field approximations use the same Non-uniform Rational B-spline (NURBS) basis functions, and the spline geometry can greatly reduce a costly mesh generation task. In addition, these functions represent exactly various complex curves and surfaces, such as toroids, spheres, and circles. The numerical solution becomes more accurate by a combination of (i) the reduction of the geometrical error, and (ii) the improved approximation properties of the NURBS basis functions in comparison with traditional piecewise polynomials. The application of the IgA for two-dimensional fatigue analysis is present in several studies coupled with X/GFEM [23, 24, 25, 26] and phase-field modelling [27]. For three-dimensional applications, Shoheib [28] applies the eXtended IgA (XIGA) to predict fatigue life of semi-elliptical cracks in welded pipelines.

In contrast to domain-based numerical methods, the Boundary Element Method (BEM) requires only a boundary discretisation for determining the mechanical fields. Besides simplifying the meshing procedure, the dimensional reduction greatly reduces issues associated with FEM and other methods due to the singular stress behaviour at the crack front. In addition, re-meshing of the boundary only occurs when the crack crosses the external boundary during crack growth procedures. The absence of a domain mesh facilitates the creation of new elements without affecting all the algebraic system. The application of BEM to two-dimensional fatigue analysis began

with Portela et al. [29], who used the Dual BEM formulation [30], which models each crack face using linearly independent boundary integral equations. Further, Mi and Aliabadi [31] pioneered the use of the BEM for three-dimensional fatigue crack growth, while subsequent studies [32, 33, 34, 35, 36] have demonstrated the robustness of this strategy for numerous fatigue analyses of complex three-dimensional components.

The boundary-only nature of the BEM makes it ideally suited for coupling with CAD in the IgA philosophy. Standard CAD models provide only a boundary representation for solids. This can be used directly for the construction of a BEM model, unlike isogeometric FEM approaches in which a (non-trivial) process of creating a NURBS volumetric model is required. In this context, in the Isogeometric BEM (IGABEM), this integration becomes straightforward, as the geometric CAD entity directly serves as the IGABEM mesh. Simpson et al. [37] were pioneers in proposing the IGABEM for two-dimensional elasticity, while following studies developed three-dimensional applications [38, 39]. Peng et al. [40] proposed three-dimensional IGABEM for fatigue crack propagation using the Paris-Erdogan Law, while Sun et al. [41] studied the influence of inclusions in the crack growth analysis with IGABEM. However, these IGABEM studies on fatigue propagation have not assessed the number of allowable cycles in their numerical analyses. In addition, the crack marching algorithm used does not allow a change in the NURBS weights, which limits the capabilities of the numerical representation of the crack front. Furthermore, they use a crack growth criterion that does not consider mode III in the crack propagation angle. Part of the novelties in the present study is the addressing of these shortcomings.

The enrichment strategy in BEM and IGABEM represents a significant advancement in numerical fracture mechanics. Simpson and Trevelyan [42, 43] expanded the partition of unity concept for fracture mechanics in the BEM, enabling accurate determination of SIFs and the mechanical behaviour of two-dimensional LEFM problems. In addition, the eXtended BEM (XBEM) strategy allows for the direct determination of the SIFs, eliminating complex post-processing tasks [44, 45]. Andrade et al. [46] performed the coupling between the IGABEM and the XBEM for two-dimensional fatigue analysis, demonstrating the formulation ability to predict the mechanical failure of several complex geometries in mixed-mode propagation response. Rocha et al. [47] proposed the three-dimensional XIGABEM for LEFM problems, where the SIFs coefficients become part of the algebraic system solution, along with improvements in the convergence rate for the studied problems.

In the present work, fatigue crack growth analysis with a three-dimensional XIGABEM formulation is presented for the first time.

In this paper, we propose a fatigue crack growth analysis algorithm for three-dimensional geometries with the XIGABEM, in which the SIFs come directly as system unknowns, eliminating the requirement for a J-integral or other approximate techniques for their extraction. This study also compares the application of the standard crack growth criterion for IGABEM (Hoop stress criterion) with a suitable criterion for mixed-mode three-dimensional behaviour (Schollmann criterion). In addition, a new crack front update algorithm is proposed, using a least-squares technique to define the corresponding NURBS curve for the updated crack front. It is worth noting that the analyses in this study assume fully linear elasticity in both the material model and the LEFM fracture framework. This is consistent with the assumptions of the Paris-Erdogan Law and accurately represents linear fatigue behavior in solids. However, in its current form, the XIGABEM formulation cannot account for nonlinear fatigue effects, such as overload phenomena.

The original aspects mentioned in the last paragraph have been presented in the following. Section 2 presents the XIGABEM formulation for three-dimensional linear elasticity and the enrichment strategy for LEFM. Section 3 discusses aspects associated with the fatigue crack growth phenomenon, such as life cycle assessment and crack growth angle. In section 4, we present the alterations required in the XIGABEM framework to account for the crack growth procedure, including the new crack front updating strategy. Next, section 5 provides three numerical applications that demonstrate the success of the proposed XIGABEM scheme in the fatigue life-cycle analysis for three-dimensional cracks.

2. Three-dimensional eXtended Isogeometric Boundary Element Method

2.1. Dual Isogeometric Boundary Element Method

The numerical solution of a three-dimensional elastostatics problem using the Boundary Element Method relies on boundary integral equations (BIEs) to represent the mechanical behaviour of the solid component solely in terms of geometry and mechanical quantities at the boundary. In problems containing cracks, when two surfaces coincide geometrically, using the general BIE for elasticity on both crack sides leads to an ill-posed problem. To address this issue, the Dual BEM [30, 48] utilises two different BIEs, one

for each crack surface, to accurately determine the mechanical quantities at these surfaces. Consider a three-dimensional cracked solid with domain Ω and boundary $\Gamma = \Gamma_{eb} \cup \Gamma_{c+} \cup \Gamma_{c-}$, where Γ_{eb} is the external boundary, and Γ_{c+} and Γ_{c-} are the opposite crack faces. For linear elasticity, the Displacement BIE (DBIE) and the Traction BIE (TBIE) relate the displacements u_k and the traction t_k when applied on a collocation point $\hat{\mathbf{x}}$ on the boundary as:

$$c_{\ell k}(\hat{\mathbf{x}})u_k(\hat{\mathbf{x}}) + \int_{\Gamma} T_{\ell k}^*(\mathbf{x}, \hat{\mathbf{x}})u_k(\mathbf{x}) d\Gamma = \int_{\Gamma} U_{\ell k}^*(\mathbf{x}, \hat{\mathbf{x}})t_k(\mathbf{x}) d\Gamma \quad (1)$$

$$\frac{1}{2}t_j(\hat{\mathbf{x}}) + n_{\ell}(\hat{\mathbf{x}}) \int_{\Gamma} S_{k\ell j}^*(\mathbf{x}, \hat{\mathbf{x}})u_k(\mathbf{x}) d\Gamma = n_{\ell}(\hat{\mathbf{x}}) \int_{\Gamma} D_{k\ell j}^*t_k(\mathbf{x}, \hat{\mathbf{x}}) d\Gamma \quad (2)$$

in which $c_{\ell k}$ is a jump term that depends on the position of the collocation point, with $c_{\ell k} = 0.5\delta_{\ell k}$ for points on a smooth boundary, $\delta_{\ell k}$ stands for the Kronecker delta, \mathbf{x} is a point on the integration boundary Γ and n_{ℓ} is the outward normal vector at $\hat{\mathbf{x}}$. The TBIE results from the differentiation of the DBIE with respect to $\hat{\mathbf{x}}$. In addition, $T_{\ell k}^*$, $U_{\ell k}^*$, $S_{k\ell j}^*$ and $D_{k\ell j}^*$ are fundamental solutions for the 3D elasticity problem, which are:

$$U_{\ell k}^*(\mathbf{x}, \hat{\mathbf{x}}) = \frac{1}{16\pi\mu(1-\nu)r} [(3-4\nu)\delta_{\ell k} + r_{,\ell r,k}] \quad (3)$$

$$T_{\ell k}^*(\mathbf{x}, \hat{\mathbf{x}}) = \frac{-1}{8\pi(1-\nu)r^2} \left\{ \frac{\partial r}{\partial \mathbf{n}} [(1-2\nu)\delta_{\ell k} + 3r_{,\ell r,k}] - (1-2\nu)(r_{,\ell}n_k + r_{,k}n_{\ell}) \right\} \quad (4)$$

$$D_{k\ell j}^*(\mathbf{x}, \hat{\mathbf{x}}) = \frac{1}{8\pi(1-\nu)r^2} [(1-2\nu)(\delta_{k\ell}r_{,j} + \delta_{jk}r_{,\ell} - \delta_{\ell j}r_{,k}) + 3(r_{,\ell r,jr,k})] \quad (5)$$

$$S_{k\ell j}^*(\mathbf{x}, \hat{\mathbf{x}}) = \frac{\mu}{4\pi(1-\nu)r^3} \left\{ 3 \frac{\partial r}{\partial \mathbf{n}} [(1-2\nu)\delta_{\ell j}r_{,k} + \nu(\delta_{\ell k}r_{,j} + \delta_{jk}r_{,\ell}) - 5r_{,\ell r,jr,k}] + 3\nu(n_{\ell}r_{,jr,k} + n_jr_{,\ell r,k}) + (1-2\nu)(3n_kr_{,\ell r,j} + n_j\delta_{\ell k} + n_{\ell}\delta_{jk}) - (1-4\nu)n_k\delta_{\ell j} \right\} \quad (6)$$

in which E and ν are the Young's Modulus and the Poisson's ratio, respectively, $\mu = \frac{E}{2(1+\nu)}$ is the shear modulus, $\mathbf{r} = \mathbf{x} - \hat{\mathbf{x}}$ is the distance vector between the collocation point and \mathbf{x} , $r = |\mathbf{r}|$, and \mathbf{n} represents the outward normal vector at \mathbf{x} .

The Dual BEM considers the application of the DBIE for collocation points on both Γ_{eb} and Γ_{c+} , while the TBIE is used for collocation points on Γ_{c-} , written as:

$$\frac{\delta_{\ell k}}{2} u_k(\hat{\mathbf{x}}^{eb}) + \int_{\Gamma} T_{\ell k}^*(\mathbf{x}, \hat{\mathbf{x}}^{eb}) u_k(\mathbf{x}) d\Gamma = \int_{\Gamma} U_{\ell k}^*(\mathbf{x}, \hat{\mathbf{x}}^{eb}) t_k(\mathbf{x}) d\Gamma \quad (7)$$

$$\begin{aligned} & \frac{\delta_{\ell k}}{2} u_k(\hat{\mathbf{x}}^{c+}) + \frac{\delta_{\ell k}}{2} u_k(\hat{\mathbf{x}}^{c-}) + \\ & \int_{\Gamma} T_{\ell k}^*(\mathbf{x}, \hat{\mathbf{x}}^{c+}) u_k(\mathbf{x}) d\Gamma = \int_{\Gamma} U_{\ell k}^*(\mathbf{x}, \hat{\mathbf{x}}^{c+}) t_k(\mathbf{x}) d\Gamma \end{aligned} \quad (8)$$

$$\begin{aligned} & \frac{1}{2} t_j(\hat{\mathbf{x}}^{c-}) - \frac{1}{2} t_j(\hat{\mathbf{x}}^{c+}) + n_{\ell}(\hat{\mathbf{x}}^{c-}) \int_{\Gamma} S_{k\ell j}^*(\mathbf{x}, \hat{\mathbf{x}}^{c-}) u_k(\mathbf{x}) d\Gamma \\ & = n_{\ell}(\hat{\mathbf{x}}^{c-}) \int_{\Gamma} D_{k\ell j}^* t_k(\mathbf{x}, \hat{\mathbf{x}}^{c-}) d\Gamma \end{aligned} \quad (9)$$

in which $\hat{\mathbf{x}}^{eb}$, $\hat{\mathbf{x}}^{c+}$ and $\hat{\mathbf{x}}^{c-}$ are the collocation points on the external boundary, upper crack face and lower crack face, respectively. In addition, the strongly-singular nature of $T_{\ell k}^*$ and $D_{k\ell j}^* t_k$ requires an integration in the Cauchy Principal Value (CPV) sense, while the hyper-singular nature of the $S_{k\ell j}^*$ kernel demands the Hadamard Finite Part (HFP) for its assessment. In eq. (7), eq. (8) and eq. (9), \int and \int represent the CPV and the HFP, respectively. The existence of coincident boundaries for representing the opposing crack faces causes additional jump terms to arise in each BIE, so the singularity in the relevant fundamental solution at both mirrored collocation points is properly considered.

The isogeometric approach is introduced to the BEM by the application of isogeometric functions for the geometrical and mechanical description, as presented in Beer et al. [49]. The NURBS surface comes from the tensor product of two univariate NURBS curves. The NURBS curve construction requires a degree p , a set of n control points P_k^i , corresponding weights w^i for each control point, and a non-decreasing knot vector $\Xi = \{\xi^1, \xi^2, \dots, \xi^{n+p+1}\}$. Then, there are several forms to define the NURBS basis functions $\phi_i(\xi)$ at the parametric coordinate ξ , and the well-established Cox-de-Boor formula [50, 51, 52] becomes suitable for the computational implementation, being:

$$\phi_i(\xi) = \frac{N_i(\xi)w_i}{\sum_{k=1}^n N_k(\xi)w_k} \quad (10)$$

$$N_{i,0}(\xi) = \begin{cases} 1 & \xi^i \leq \xi < \xi^{i+1} \\ 0 & \text{otherwise} \end{cases} \quad (11)$$

$$N_{i,p}(\xi) = \frac{\xi - \xi^i}{\xi^{i+p} - \xi^i} N_{i,p-1}(\xi) + \frac{\xi^{i+p+1} - \xi}{\xi^{i+p+1} - \xi^{i+1}} N_{i+1,p-1}(\xi) \quad (12)$$

in which the index after the comma refers to the degree of the B-Spline and NURBS basis function, following the standard notation of Piegl et al. [53].

The tensor product of a NURBS curve of degree p , with n control points, and knot vector $\Xi_1 = \{\xi_1^1, \xi_1^2, \dots, \xi_1^{n+p+1}\}$ with a NURBS curve having degree q , m control points and knot vector $\Xi_2 = \{\xi_2^1, \xi_2^2, \dots, \xi_2^{m+q+1}\}$ results in a NURBS surface whose basis function is:

$$\phi_\alpha(\xi_1, \xi_2) = \frac{N_i(\xi_1) M_j(\xi_2) w_\alpha}{\sum_{k=1}^n \sum_{l=1}^m N_k(\xi_1) M_l(\xi_2) w_\alpha} \quad (13)$$

in which N and M stand for each parametric direction, α is a connectivity index referring to the uni-variate basis function indices i and j of each NURBS curve and w_α is the corresponding weight. Then, the geometrical description and the mechanical fields interpolations in a patch γ are:

$$x_k^\gamma(\xi_1, \xi_2) = \sum_{\alpha=1}^{n^\gamma} \phi_\alpha^\gamma(\xi_1, \xi_2) P_k^\beta \quad (14)$$

$$u_k^\gamma(\xi_1, \xi_2) = \sum_{\alpha=1}^{n^\gamma} \phi_\alpha^\gamma(\xi_1, \xi_2) d_k^\beta \quad (15)$$

$$t_k^\gamma(\xi_1, \xi_2) = \sum_{\alpha=1}^{n^\gamma} \phi_\alpha^\gamma(\xi_1, \xi_2) p_k^\beta \quad (16)$$

in which β is a global connectivity index associated with α and γ , P_k^β are the control points coordinates responsible for defining the NURBS surfaces, d_k^β and p_k^β are the displacement and traction coefficients for the interpolation of these mechanical fields. Both d_k^β and p_k^β no longer possess physical meaning, while they still have appropriate units, since the control points are not necessarily on the boundary. However, boundary values of displacement and traction components may be simply recovered from these coefficients (once

they become known) through application of eq. (15) and eq. (16). In addition, this lack of physical meaning requires care to be taken in the application of non-constant boundary conditions.

The numerical integration required by the BIEs can be performed using the standard Gauss-Legendre quadrature in the non-singular regions, which demands a mapping between the physical space and the integration space $\{\hat{\xi}_1, \hat{\xi}_2 \in \Lambda \mid \Lambda = [-1; 1] \times [-1; 1]\}$. This occurs in two steps, in which the first is the correspondence between the physical space and the parametric space (eq. (14)) and the second is a coordinate transformation between the NURBS parametric space of a knot span $[\xi_1^i, \xi_1^{i+1}] \times [\xi_2^j, \xi_2^{j+1}]$ and the integration space as:

$$\xi_1 = \frac{(\xi_1^{i+1} - \xi_1^i) \hat{\xi}_1 + (\xi_1^{i+1} + \xi_1^i)}{2} \quad (17)$$

$$\xi_2 = \frac{(\xi_2^{j+1} - \xi_2^j) \hat{\xi}_2 + (\xi_2^{j+1} + \xi_2^j)}{2} \quad (18)$$

Then, in the isogeometric approach two Jacobians, J_1 and J_2 , arise in the boundary integration, as:

$$d\Gamma = J_1 J_2 d\Lambda = J d\Lambda \quad (19)$$

$$J_1 = \left\| \frac{\partial \mathbf{r}}{\partial \xi_1} \times \frac{\partial \mathbf{r}}{\partial \xi_2} \right\| \quad (20)$$

$$J_2 = \frac{(\xi_1^{i+1} - \xi_1^i)}{2} \frac{(\xi_2^{j+1} - \xi_2^j)}{2} \quad (21)$$

in which J is the total Jacobian of the transformation. Knot spans containing the collocation point require a different approach since the kernels exhibit a singular behaviour in them. In this study, the numerical assessment of these strongly-singular and hyper-singular integrals uses the Singularity Subtraction Technique (SST) [54, 55], based on a polar transformation around the singularity, the expansion in Taylor series of the singular integrand and a semi-analytical integration in the circumferential direction. Additionally, the HFP requires a C^1 continuity for the integrand in the vicinity of the collocation point. Cordeiro and Leonel [56] present the expanded terms in a detailed form of the SST for the three-dimensional IGABEM.

The introduction of the geometry, displacement and traction interpolation shown in eq. (14), eq. (15) and eq. (16) into the BIEs, leads to a set of equations written in a discretised form as:

$$\frac{\delta_{\ell k}}{2} \sum_{\alpha=1}^{n^\gamma} \phi_\alpha^{\hat{\gamma}}(\hat{\mathbf{x}}^{eb}) d_k^\beta + \sum_{\gamma=1}^{NS} \underline{\mathbb{T}}_{\ell k}^{*\alpha\gamma} d_k^\beta = \sum_{\gamma=1}^{NS} \underline{\mathbb{U}}_{\ell k}^{*\alpha\gamma} p_k^\beta \quad (22)$$

$$\frac{\delta_{\ell k}}{2} \sum_{\alpha=1}^{n^\gamma} \phi_\alpha^{\hat{\gamma}^+}(\hat{\mathbf{x}}^{c^+}) d_k^\beta + \frac{\delta_{\ell k}}{2} \sum_{\alpha=1}^{n^\gamma} \phi_\alpha^{\hat{\gamma}^-}(\hat{\mathbf{x}}^{c^-}) d_k^\beta + \sum_{\gamma=1}^{NS} \underline{\mathbb{T}}_{\ell k}^{*\alpha\gamma} d_k^\beta = \sum_{\gamma=1}^{NS} \underline{\mathbb{U}}_{\ell k}^{*\alpha\gamma} p_k^\beta \quad (23)$$

$$\begin{aligned} & \frac{1}{2} \sum_{\alpha=1}^{n^\gamma} \phi_\alpha^{\hat{\gamma}^-}(\hat{\mathbf{x}}^{c^-}) p_j^\beta - \frac{1}{2} \sum_{\alpha=1}^{n^\gamma} \phi_\alpha^{\hat{\gamma}^+}(\hat{\mathbf{x}}^{c^+}) p_j^\beta \\ & + n_\ell(\hat{\mathbf{x}}^{c^-}) \sum_{\gamma=1}^{NS} \underline{\mathbb{S}}_{k\ell j}^{*\alpha\gamma} d_k^\beta = n_\ell(\hat{\mathbf{x}}) \sum_{\gamma=1}^{NS} \underline{\mathbb{D}}_{k\ell j}^{*\alpha\gamma} p_k^\beta \end{aligned} \quad (24)$$

in which $\hat{\mathbf{x}}$ represents a point on the NURBS surface containing the collocation point. The arguments of the fundamental kernels are now omitted for brevity. In addition, $\underline{\mathbb{T}}_{\ell k}^{*\alpha\gamma}$, $\underline{\mathbb{U}}_{\ell k}^{*\alpha\gamma}$, $\underline{\mathbb{S}}_{k\ell j}^{*\alpha\gamma}$ and $\underline{\mathbb{D}}_{k\ell j}^{*\alpha\gamma}$ are:

$$\underline{\mathbb{T}}_{\ell k}^{*\alpha\gamma} = \sum_{\text{ks}=1}^{n_{\text{ks}}^\gamma} \int_{\Lambda} T_{\ell k}^* \phi_\alpha^\gamma J_\gamma^{\text{ks}} d\Lambda \quad (25)$$

$$\underline{\mathbb{U}}_{\ell k}^{*\alpha\gamma} = \sum_{\text{ks}=1}^{n_{\text{ks}}^\gamma} \int_{\Lambda} U_{\ell k}^* \phi_\alpha^\gamma J_\gamma^{\text{ks}} d\Lambda \quad (26)$$

$$\underline{\mathbb{S}}_{k\ell j}^{*\alpha\gamma} = \sum_{\text{ks}=1}^{n_{\text{ks}}^\gamma} \int_{\Lambda} S_{k\ell j}^* \phi_\alpha^\gamma J_\gamma^{\text{ks}} d\Lambda \quad (27)$$

$$\underline{\mathbb{D}}_{k\ell j}^{*\alpha\gamma} = \sum_{\text{ks}=1}^{n_{\text{ks}}^\gamma} \int_{\Lambda} D_{k\ell j}^* \phi_\alpha^\gamma J_\gamma^{\text{ks}} d\Lambda \quad (28)$$

in which ks denotes the knot span and n_{ks}^γ is the number of knot spans in the patch γ .

The discretised form of the elastostatic boundary value problem has a total of $3N_d$ and $3N_p$ displacement and traction coefficients, respectively, with $N_d = N_p = N_{\text{coeff}}$ when both fields use the same discretisation. Half of these coefficients come directly from the boundary conditions applied, while the another half is unknown due to $\Gamma_u \cap \Gamma_p = \emptyset$. In this sense, the problem has N_{coeff} unknowns mixed between \mathbf{d} and \mathbf{p} . The algebraic system

containing N_{coeff} equations come from the application of eq. (22), eq. (23), and eq. (24) on the same number of unknowns. Then, the standard procedure for the IGABEM is to determine the position of N_{coeff} collocation points in the entire boundary based on the Greville Abscissae strategy [57]. Considering each control point α in a NURBS surface γ , its equivalent collocation pair in the parametric space $(\xi_1^i, \xi_2^j)^{\alpha\gamma}$ is:

$$(\hat{\xi}_1^i)^{\alpha\gamma} = \frac{\sum_{s=i+1}^{i+p} \xi_1^s}{p} \quad (29)$$

$$(\hat{\xi}_2^j)^{\alpha\gamma} = \frac{\sum_{s=j+1}^{j+q} \xi_2^s}{q} \quad (30)$$

in which i and j are the indices of the uni-variate NURBS curve that generates the NURBS surface and ξ_1^s and ξ_2^s come from their knot vectors. To ensure that all collocation points are on smooth boundaries, as well as C^1 continuity for all points lying on the crack surfaces, a repositioning strategy alters their position. For a knot span $[\xi_1^i, \xi_1^{i+1}] \times [\xi_2^j, \xi_2^{j+1}]$, this replacement occurs when $(\xi_1^i, \xi_2^j)^{\alpha\gamma}$ are at the end of the NURBS surface knot span or if there is a knot multiplicity in that knot span so that C^1 continuity cannot be guaranteed, as:

$$(\xi_1^{i\text{alt}})^{\alpha\gamma} = (\xi_1^i)^{\alpha\gamma} \pm 0.1(\xi_1^{i+1} - \xi_1^i) \quad (31)$$

$$(\xi_2^{j\text{alt}})^{\alpha\gamma} = (\xi_2^j)^{\alpha\gamma} \pm 0.1(\xi_2^{j+1} - \xi_2^j) \quad (32)$$

in which the \pm sign corresponds to forward or backward movement, depending on whether the collocation point lies on the beginning or on the end of the knot span.

After applying eq. (22), eq. (23) and eq. (24), to all of the collocation points generated by the Greville Abscissae strategy, the algebraic system may be written:

$$\begin{bmatrix} \mathbf{H}^{\text{eb}} \\ \mathbf{H}^{\text{c}^+} \\ \mathbf{H}^{\text{c}^-} \end{bmatrix} \begin{bmatrix} \mathbf{d}^{\text{eb}} \\ \mathbf{d}^{\text{c}^+} \\ \mathbf{d}^{\text{c}^-} \end{bmatrix} = \begin{bmatrix} \mathbf{G}^{\text{eb}} \\ \mathbf{G}^{\text{c}^+} \\ \mathbf{G}^{\text{c}^-} \end{bmatrix} \begin{bmatrix} \mathbf{p}^{\text{eb}} \\ \mathbf{p}^{\text{c}^+} \\ \mathbf{p}^{\text{c}^-} \end{bmatrix} \Rightarrow \mathbf{H}\mathbf{d} = \mathbf{G}\mathbf{t} \quad (33)$$

where \mathbf{H}^{eb} and \mathbf{G}^{eb} are the influence factors of displacements and tractions of the external boundary, \mathbf{H}^{c^+} and \mathbf{G}^{c^+} correspond to the upper crack face while \mathbf{H}^{c^-} and \mathbf{p}^{c^-} are the equivalent for the lower crack face.

Boundary conditions are applied by introducing suitable values for the displacement and traction coefficients in eq. (33). For constant boundary conditions, the single application of its value as the coefficient is enough to describe the boundary condition fully. However, non-constant distributions pose an issue for isogeometric approaches, in which alternative strategies, such as direct integration of the entire kernel substituting the correspondent analytical expression or a least square approximation overcome the problem. In this study, for simplicity, solely constant boundary conditions are present. After applying the boundary condition coefficients in eq. (33), the IGABEM algebraic system becomes similar to its BEM counterpart, as:

$$\mathbf{Ax} = \mathbf{b} \quad (34)$$

in which the \mathbf{A} matrix contains all influence factors, \mathbf{x} contains the unknowns displacement and traction coefficients and \mathbf{b} is a right-hand side vector which results from applying the boundary conditions on the general form of the IGABEM.

2.2. Crack front enrichment strategy for direct assessment of the SIFs

The use of NURBS basis functions in IGABEM improves the geometrical representation of the solid, which reduces the influence of errors that arise from the standard Lagrangian basis functions to describe the geometry. However, like the piecewise polynomials in the conventional BEM, the NURBS functions used in the IGABEM cannot adequately capture the \sqrt{r} behaviour in the displacement in the vicinity of the crack front. As a consequence, when both dual BEM and IGABEM formulations are used to solve fracture mechanics problem, a non-physical gap in the crack front emerges, and this displacement discontinuity accounts for the majority of the overall error in the solution. To circumvent this problem, the proper introduction of the \sqrt{r} in the solution field as an enriching function results in the tying between the crack surfaces at the crack front. This strategy may be labelled the eXtended IGABEM (XIGABEM) approach, as firstly proposed Rocha et al. [47] for three-dimensional linear elastic fracture mechanics. The introduction of the \sqrt{r} behaviour at the crack surfaces and the absence of the non-physical displacement discontinuity give rise to improvements in the convergence rate in comparison to the conventional IGABEM. Mathematically, the displacement field in eq. (15) includes an enriching term as:

$$u_k^{\gamma^{c+/-}}(\xi_1, \xi_2) = \sum_{\alpha=1}^{n^\gamma} \phi_\alpha^{\gamma^{c+/-}}(\xi_1, \xi_2) d_k^\beta + \sum_{s=1}^{n_K^\gamma} R_{kq}^{\text{cf}} \psi_{qM}^{\gamma^{\text{cf}}} \tilde{\phi}_s^{\text{cf}}(v) \tilde{K}_M^{s\text{cf}} \quad (35)$$

in which $\gamma^{c+/-}$ is the upper or lower crack face containing the crack front, while $\tilde{\phi}_s^{\text{cf}}(v)$ is a set of NURBS basis functions at the crack front, which are the same as the uni-variate basis functions of the NURBS surface in the corresponding direction and with parametric coordinate v . The term $\psi_{qM}^{\gamma^{\text{cf}}}$ is the enrichment function inspired in the first term of the Williams expansion as:

$$\psi_{qM} = \begin{bmatrix} \psi_{nI} & \psi_{nII} & \psi_{nIII} \\ \psi_{bI} & \psi_{bII} & \psi_{bIII} \\ \psi_{tI} & \psi_{tII} & \psi_{tIII} \end{bmatrix} \quad (36)$$

$$\psi_{nI} = \frac{1}{2\mu} \sqrt{\frac{r^t}{2\pi}} \cos\left(\frac{\theta^t}{2}\right) \left[\kappa - 1 + 2 \sin^2\left(\frac{\theta^t}{2}\right) \right] \quad (37)$$

$$\psi_{nII} = \frac{1}{2\mu} \sqrt{\frac{r^t}{2\pi}} \sin\left(\frac{\theta^t}{2}\right) \left[\kappa + 1 + 2 \cos^2\left(\frac{\theta^t}{2}\right) \right] \quad (38)$$

$$\psi_{bI} = \frac{1}{2\mu} \sqrt{\frac{r^t}{2\pi}} \sin\left(\frac{\theta^t}{2}\right) \left[\kappa + 1 - 2 \cos^2\left(\frac{\theta^t}{2}\right) \right] \quad (39)$$

$$\psi_{bII} = -\frac{1}{2\mu} \sqrt{\frac{r^t}{2\pi}} \cos\left(\frac{\theta^t}{2}\right) \left[\kappa - 1 - 2 \sin^2\left(\frac{\theta^t}{2}\right) \right] \quad (40)$$

$$\psi_{tIII} = \frac{1}{2\mu} \sqrt{\frac{r^t}{2\pi}} 4 \sin\left(\frac{\theta^t}{2}\right) \quad (41)$$

$$\psi_{tI} = \psi_{tII} = \psi_{nIII} = \psi_{bIII} = 0 \quad (42)$$

in which r^t are geometrical properties related to the point $P(\xi_1, \xi_2)$ at the enriched surface depicted in fig. 1. κ is the Kolosov constant associated to the crack front stress state, being $\kappa = 3 - 4\nu$ for plane-strain and $\kappa = \frac{3-\nu}{1+\nu}$ for plane-stress. This set of enrichment functions resembles those in Oden-Duarte [58, 59]. However, in the XIGABEM approach, they are combined with the rotation matrix R_{kq}^{cf} so that the additional unknowns $\tilde{K}_M^{s\text{cf}}$ become stress intensity factors parameters. The rotation matrix R_{kq}^{cf} contains the local coordinate system $[\vec{N} \vec{B} \vec{T}]$ in fig. 1 and transforms the terms of the

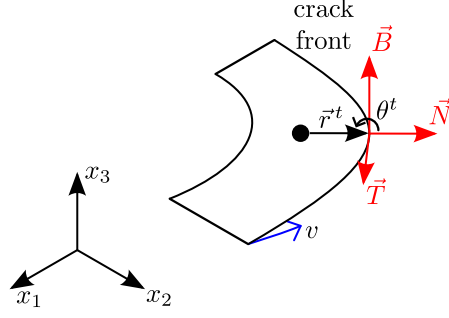


Figure 1: Local coordinate system and enrichment terms definition for crack front enrichment scheme.

enrichment function from the local coordinate system at the crack front to the global coordinate system of the problem. For the isogeometric approach, this study uses the Frenet-Serret frame [60, 61] to determine R_{kq}^{cf} , which is a suitable framework since in IgA it may be directly derived as function of the NURBS curve properties and its derivatives.

The augmented displacement field of the eq. (35) replaces the standard isogeometric approximation for this field to obtain the XIGABEM algebraic system. As a result, new terms arise in the discretised set of equations while the other terms of the standard IGABEM are not affected. Then, by proceeding in a similar fashion as for the IGABEM, but with the enriched field, the discretised set of equations becomes:

$$\frac{\delta_{\ell k}}{2} \sum_{\alpha=1}^{n^\gamma} \phi_\alpha^{\hat{\gamma}}(\hat{\mathbf{x}}^{eb}) d_k^\beta + \sum_{\gamma=1}^{NS} \mathbb{T}_{\ell k}^{*\alpha\gamma} d_k^\beta + \sum_{\gamma=1}^{NS} \mathbb{T}_{s\ell M}^{scf} \tilde{K}_M^{scf} = \sum_{\gamma=1}^{NS} \mathbb{U}_{\ell k}^{*\alpha\gamma} p_k^\beta \quad (43)$$

$$\begin{aligned}
& \frac{\delta_{\ell k}}{2} \sum_{\alpha=1}^{n^\gamma} \phi_{\alpha}^{\hat{\gamma}+}(\hat{\mathbf{x}}^{c+}) d_k^\beta + \frac{\delta_{\ell k}}{2} \sum_{\alpha=1}^{n^\gamma} \phi_{\alpha}^{\hat{\gamma}-}(\hat{\mathbf{x}}^{c-}) d_k^\beta \\
& + \frac{\delta_{\ell k}}{2} \sum_{s=1}^{n_K^\gamma} \tilde{\phi}_s^{\text{cf}}(v(\hat{\mathbf{x}}^{c+})) R_{kq}^{\text{cf}}(\hat{\mathbf{x}}^{c+}) \psi_{qM}^{\hat{\gamma}\text{cf}}(\hat{\mathbf{x}}^{c+}) \tilde{K}_M^{s\text{cf}} \\
& + \frac{\delta_{\ell k}}{2} \sum_{s=1}^{n_K^\gamma} \tilde{\phi}_s^{\text{cf}}(v(\hat{\mathbf{x}}^{c-})) R_{kq}^{\text{cf}}(\hat{\mathbf{x}}^{c-}) \psi_{qM}^{\hat{\gamma}\text{cf}}(\hat{\mathbf{x}}^{c-}) \tilde{K}_M^{s\text{cf}} \\
& + \sum_{\gamma=1}^{NS} \underline{\mathbb{T}}_{\ell k}^{*\alpha\gamma} d_k^\beta + \sum_{\gamma=1}^{NS} \underline{\mathbb{T}}_{s\ell M}^{s\text{cf}} \tilde{K}_M^{s\text{cf}} = \sum_{\gamma=1}^{NS} \underline{\mathbb{U}}_{\ell k}^{*\alpha\gamma} p_k^\beta
\end{aligned} \tag{44}$$

$$\begin{aligned}
& \frac{1}{2} \sum_{\alpha=1}^{n^\gamma} \phi_{\alpha}^{\hat{\gamma}-}(\hat{\mathbf{x}}^{c-}) p_j^\beta - \frac{1}{2} \sum_{\alpha=1}^{n^\gamma} \phi_{\alpha}^{\hat{\gamma}+}(\hat{\mathbf{x}}^{c+}) p_j^\beta \\
& + n_\ell(\hat{\mathbf{x}}^{c-}) \sum_{\gamma=1}^{NS} \underline{\mathbb{S}}_{k\ell j}^{*\alpha\gamma} d_k^\beta + n_\ell(\hat{\mathbf{x}}^{c-}) \sum_{\gamma=1}^{NS} \underline{\mathbb{S}}_{s\ell j M}^{s\text{cf}} \tilde{K}_M^{s\text{cf}} = n_\ell(\hat{\mathbf{x}}^{c-}) \sum_{\gamma=1}^{NS} \underline{\mathbb{D}}_{k\ell j}^{*\alpha\gamma} p_k^\beta
\end{aligned} \tag{45}$$

in which new jump terms only arise on the DBIE applied at the upper crack faces. In addition, the terms $\underline{\mathbb{T}}_{s\ell M}^{s\text{cf}}$ and $\underline{\mathbb{S}}_{s\ell j M}^{s\text{cf}}$ correspond to the influence of the enrichment terms on the fundamental kernels as:

$$\underline{\mathbb{T}}_{s\ell M}^{s\text{cf}} = \sum_{\text{ks}=1}^{n_{\text{ks}}^{\gamma(\text{cf})}} \int_{\Lambda} T_{\ell k}^* \tilde{\phi}_s^{\text{cf}} R_{kq}^{\text{cf}} \psi_{qM}^{\gamma(\text{cf})} J_{\gamma(\text{cf})}^{\text{ks}} d\Lambda \tag{46}$$

$$\underline{\mathbb{S}}_{s\ell j M}^{s\text{cf}} = \sum_{\text{ks}=1}^{n_{\text{ks}}^{\gamma(\text{cf})}} \int_{\Lambda} S_{k\ell j}^* \tilde{\phi}_s^{\text{cf}} R_{kq}^{\text{cf}} \psi_{qM}^{\gamma(\text{cf})} J_{\gamma(\text{cf})}^{\text{ks}} d\Lambda \tag{47}$$

The evaluation of boundary integrals requires us to locate the point at the crack front with minimum distance to the integration point, and a point projection algorithm [53] is used to find the corresponding parametric coordinate of this point. The kernels contained in the integrals inherit the order of singularity of their counterparts in the standard IGABEM, i.e. the enrichment causes no increase in order of singularity. Therefore, the CPV and the HFP are responsible for their regularisation in a similar procedure to that in the IGABEM. The expansion of each term in the regularisation is present in the appendix B of the work of Rocha et al. [47].

New unknown parameters have emerged in the above development of the enriched approximation so, since we adopt a collocation-based implementation rather than Galerkin, some auxiliary equations are required to be generated to recover a square system. A suitable approach is a crack tying constraint, constraining the upper and lower crack faces at the crack front to have equal displacements (i.e. enforcing continuity of displacement), which may be applied weakly as:

$$\int_{\Gamma_s^{\text{cf}}} \left[\sum_{\alpha=1}^{n_\gamma} \phi_\alpha^{\tilde{\gamma}^+}(\xi_1, \xi_2) d_k^{\beta^+} - \sum_{\alpha=1}^{n_\gamma} \phi_\alpha^{\tilde{\gamma}^-}(\xi_1, \xi_2) d_k^{\beta^-} \right] \tilde{\phi}_s^{\text{cf}}(v) dv = 0_k \quad (48)$$

in which Γ_s^{cf} is the crack front and $\tilde{\phi}_s^{\text{cf}}$ are the weighting functions that, for this approach, are the NURBS basis functions of the uni-variate NURBS curve representing the crack front.

The final algebraic system considering the enriched IGABEM system becomes:

$$\begin{bmatrix} \mathbf{H} & \mathbf{H}_s \\ \mathbf{\Phi}_s & \mathbf{0} \end{bmatrix} \begin{Bmatrix} \mathbf{d} \\ \tilde{\mathbf{K}} \end{Bmatrix} = \begin{bmatrix} \mathbf{G} \\ \mathbf{0} \end{bmatrix} \{ \mathbf{p} \} \quad (49)$$

in which the sub-matrix \mathbf{H}_s contains the contributions from the new XI-GABEM integrals, $\mathbf{\Phi}_s$ corresponds to the coefficients from the compatibility equations eq. (48) and $\tilde{\mathbf{K}}$ contains the new enrichment parameters. The application of boundary conditions on eq. (49) results in a final system $\mathbf{Ax} = \mathbf{b}$, and a standard solver computes all the unknowns of the vector \mathbf{x} . A remarkable advantage of this formulation is its ease in the coupling with existing IGABEM codes. As noticed by the expansion of the algebraic form of the XIGABEM system in comparison to the IGABEM, the enrichment strategy does not affect the standard IGABEM terms, so the computational routines remain the same.

Another advantage of the XIGABEM enrichment is the direct extraction of the SIFs. The construction of the enrichment space results in the terms $\tilde{\mathbf{K}}$, arising in the solution vector \mathbf{x} , from which the SIFs can be readily computed as:

$$K_M^{\text{cf}}(v) = \sum_{s=1}^{n_K^\gamma} \tilde{\phi}_s^{\text{cf}}(v) \tilde{K}_M^{s\text{cf}} \quad (50)$$

thus dismissing a post-processing task that can be computationally demanding, such as the J-integral, or approximated techniques such as the Displacement Extrapolation Technique.

3. Fatigue crack propagation

Fatigue crack growth analysis with the LEFM is suitable for high-cycle loading scenarios. In this situation, the load amplitude is small enough not to cause material failure for a small amount of loading cycles, but it causes degradation through crack growth throughout the component life cycle. For LEFM to be admissible, it is assumed that the inelastic process zone ahead of the crack is negligible in size in comparison to the crack length and to the solid dimensions. Therefore, the formulation proposed herein does not take account of the nonlinear processes at the fracture process zone and the energy dissipated during fatigue has been totally utilised for creating additional crack surfaces. The life prediction analysis then relies on empirical laws that relate the crack growth rate to the variation of the stress intensity factors over the load cycle. Because of its simplicity, the Paris-Erdogan Law is commonly applied for this type of problem, and is adopted in the current work. It is noted that other crack growth laws may be applied if desired within the XIGABEM framework.

3.1. The Paris-Erdogan Law and fatigue life prediction

The Paris-Erdogan Law relates empirically the rate between the crack growth rate da/dN and the SIF range ΔK as:

$$\frac{da}{dN} = C(\Delta K)^m \quad (51)$$

in which C and m are material parameters for fatigue crack growth, whose determination relies on experimental studies. In a fully three-dimensional case, ΔK accounts for the equivalent SIF during a load cycle, which is a combination of the SIF of each mode. Then, the crack growth criterion choice defines the equivalent SIF ΔK_{eq} . This study compares the use of two criteria: the hoop stress criterion [62] and the Schollmann criterion [63]. The expressions for both the ΔK_{eq} and the propagation angle are present in section 3.2.

The classical approach of determining the required amount of cycles for the crack to grow from a length a to a length $a + \Delta a$ uses a constant approximation for the equivalent SIF variation so that $\Delta K_{eq} = K_{eq}(a + \Delta a) - K_{eq}(a)$,

which may be used directly in eq. (51). Alternatively, this study uses the linear SIF approximation for the development of the eq. (51), firstly proposed by Andrade and Leonel [64]. The study of Cordeiro and Leonel [36] applied this strategy for the three-dimensional BEM in a mixed-mode crack growth analysis, in which results have shown its advantages over the classical approach. In this context, the approximation of the equivalent SIF between the crack lengths a and $a + \Delta a$ is:

$$\Delta K_{eq} = \beta a + \gamma \quad (52)$$

in which β and γ are constants of the linear form as:

$$\beta = \frac{\Delta K_{eq}(a + \Delta a) - \Delta K_{eq}(a)}{\Delta a} \quad (53)$$

$$\gamma = \Delta K_{eq}(a) - \beta a \quad (54)$$

The substitution of the eq. (52) in the Paris-Erdogan Law, eq. (51) and its integration result in:

$$\begin{aligned} dN &= \frac{da}{C(\Delta \bar{K}_{eq})^m} \Rightarrow \\ N(a + \Delta a) - N(a) &= \Delta N = \int_a^{a+\Delta a} \frac{1}{C[\Delta K_{eq}(a)]^m} da \Rightarrow \\ \Delta N &= \frac{1}{C} \int_a^{a+\Delta a} (\beta a + \gamma)^{-m} da \Rightarrow \\ \Delta N &= \frac{1}{C} \left[\frac{(\beta a + \gamma)^{1-m}}{(1-m)\beta} \right]_a^{a+\Delta a} \Rightarrow \\ \Delta N &= \frac{\Delta a \{ [\Delta K_{eq}(a + \Delta a)]^{1-m} - [\Delta K_{eq}(a)]^{1-m} \}}{C(1-m)[\Delta K_{eq}(a + \Delta a) - \Delta K_{eq}(a)]} \end{aligned} \quad (55)$$

in which ΔN stands for the increment in the number of cycles in the crack advancement from a to $a + \Delta a$. Cordeiro and Leonel [36] have shown that this alternative formulation allows for the use of higher crack growth steps Δa in comparison to the classical approach. This enables a reduction in the computational cost by reducing the mesh density.

Finally, the total number of cycles of loading and unloading becomes the sum of each ΔN of all propagation steps of the analysis. In a computational assessment of the life cycle, the maximum increment Δa_{\max} occurs at the

crack front location with maximum ΔK_{eq}^{\max} . The advancement for each point \mathbf{x}_i at the crack front considers a weighting factor based on the Paris-Erdogan Law in a discrete manner as:

$$\Delta a(\mathbf{x}_i) = \Delta a_{\max} \left(\frac{\Delta K_{eq}(\mathbf{x}_i)}{\Delta K_{eq}^{\max}} \right)^m \quad (56)$$

in which ΔK_{eq}^{\max} is the maximum $\Delta K_{eq}(\mathbf{x}_i)$ at the crack front for the current propagation step.

3.2. Crack growth criteria

The crack growth criterion is responsible for defining the crack propagation angle θ_p associated to the local coordinate system at the crack front to define the new crack front location. Several studies have proposed techniques to define the proper crack path considering the mechanical response, the type of loading and the thermodynamics of the fracture process. For the LEFM in particular, either a global or local energy balance may be capable of describing this phenomenon. Both techniques rely on the SIFs to represent the stress state at the crack front, which in this work are directly defined with the solution of the boundary value problem for each crack increment. In this study, the choice of the maximum hoop stress criterion [62] stems from its use in previous studies of three-dimensional IGABEM crack propagation [40, 41, 65]. However, since the maximum hoop stress criterion does not consider the Mode III in the crack propagation angle, in this study we also test the Schollmann criterion [63]. We present a fully three-dimensional criterion allows for the correct computing of the crack front angle, which may be seen as a novelty in comparison to previous works in the IGABEM field. The brittle failure of the material occurs when $K_{eq} \geq K_{Ic}$, in which K_{Ic} is the material toughness for both criteria.

3.2.1. Maximum hoop stress criterion

The maximum hoop stress criterion seeks the direction in which the hoop stress is maximised for a given loading scenario. This occurs for an angle θ_p so that:

$$\theta_p = 2 \arctan \left[\frac{-2(K_{II}/K_I)}{1 + \sqrt{1 + 8(K_{II}/K_I)^2}} \right] \quad (57)$$

and the equivalent SIF K_{eq} that incorporates the mode III effects according to Gestle [66] is:

$$K_{eq} = \sqrt{K_I^2 + K_{II}^2 + (1 + \nu)K_{III}^2} \quad (58)$$

While the K_{eq} contains the influence of mode III through K_{III} , the crack propagation angle does not take this mode into account. Thus, mixed-mode fracture problems having a non-zero mode III component may not be properly represented by this criterion.

3.2.2. Schollmann criterion

The Schollmann criterion [63] defines the propagation angle such that it maximises the principal stress σ'_1 in the local coordinate system defined on the crack front. The principal stress value is:

$$\sigma'_1 = \frac{\sigma_\theta + \sigma_{\bar{x}3}}{2} + \frac{\sqrt{(\sigma_\theta + \sigma_{\bar{x}3})^2 + 4(\tau_{\theta\bar{x}3})^2}}{2} \quad (59)$$

in which all stress variables are written according to a local coordinate system at the crack front, as shown in fig. 2 and are related to the SIFs. By assuming that the component $\sigma_{\bar{x}3}$ does not affect the propagation angle, the Schollmann criterion takes $\sigma_{\bar{x}3} = 0$. Then, for three-dimensional approaches the equivalent SIF is:

$$K_{eq} = \frac{1}{2} \cos\left(\frac{\theta_p}{2}\right) \left\{ K_I \cos^2\left(\frac{\theta_p}{2}\right) - \frac{3}{2} K_{II} (\sin \theta_p) + \sqrt{\left[K_I \cos^2\left(\frac{\theta_p}{2}\right) - \frac{3}{2} K_{II} (\sin \theta_p) \right]^2 + 4K_{III}^2} \right\} \quad (60)$$

and the propagation angle θ_p may be found from:

$$\Theta = \frac{1}{8\sqrt{2\pi r}} \left\{ \frac{-K_I \bar{S}}{2} - K_{II} \bar{C}_1 + \frac{1}{2} [2 [(K_I \bar{C}_2 - K_{II} \bar{S}) - K_{II} \bar{C}_1] \left[\frac{-K_I \bar{S}}{2} - K_{II} \bar{C}_1 \right] - 16K_{III}^2 \sin(\theta_p)] \right. \quad (61)$$

$$\left. \left[[K_I \bar{C}_2 - K_{II} \bar{S}]^2 + 64K_{III}^2 \cos^2\left(\frac{\theta_p}{2}\right) \right]^{-\frac{1}{2}} \right\} = 0$$

$$\bar{C}_1 = \frac{3}{2} \cos\left(\frac{\theta_p}{2}\right) + \frac{9}{2} \cos\left(\frac{3\theta_p}{2}\right) \quad (62)$$

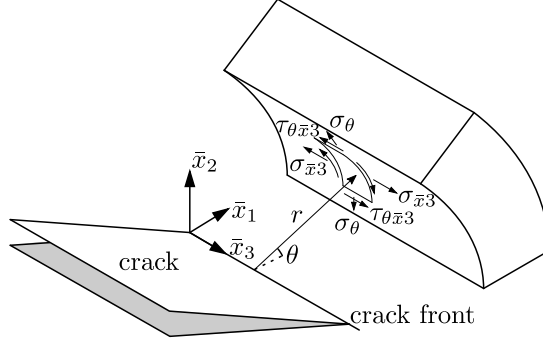


Figure 2: Local coordinate system for the crack front stresses.

$$\bar{C}_2 = 3 \cos\left(\frac{\theta_p}{2}\right) + \cos\left(\frac{3\theta_p}{2}\right) \quad (63)$$

$$\bar{S} = 3 \sin\left(\frac{\theta_p}{2}\right) + 3 \sin\left(\frac{3\theta_p}{2}\right) \quad (64)$$

There is no analytical solution for the eq. (61), but θ_p may be determined numerically. This study applies the Golden Section algorithm to determine the propagation angle. In addition, the Schollmann criterion defines the twist angle ψ_p as:

$$\psi_p = \frac{1}{2} \arctan\left[\frac{2\tau_{\theta\bar{x}3}(\theta_p)}{\sigma_{\theta}(\theta_p) - \sigma_{\bar{x}3}(\theta_p)}\right] \quad (65)$$

The twist angle influence on the XFEM [17] and in the BEM [36] relies on a crack front equivalent element. Both studies considered a linear approximation for this element, while in this study NURBS curves represent the crack front. There is therefore no natural equivalence for these strategies. In this study a zero twisting angle is assumed for simplicity; its influence on the crack front propagation within XIGABEM is suggested as a possible avenue for future work.

4. Crack propagation framework in XIGABEM

4.1. Crack front update algorithm

In a crack growth framework within the XIGABEM, the definition of the propagation angle and the increment for the crack front takes place considering the solution of the boundary value problem for the previous geometry. Then, in a numerical framework, a new set of points defining the crack front are the starting point to determine a parametric curve that best represent them. Previous studies [40, 41] for the crack growth in IGABEM applied a crack front updating algorithm proposed by LaGreca et al. [67] based on the movement of the existing control

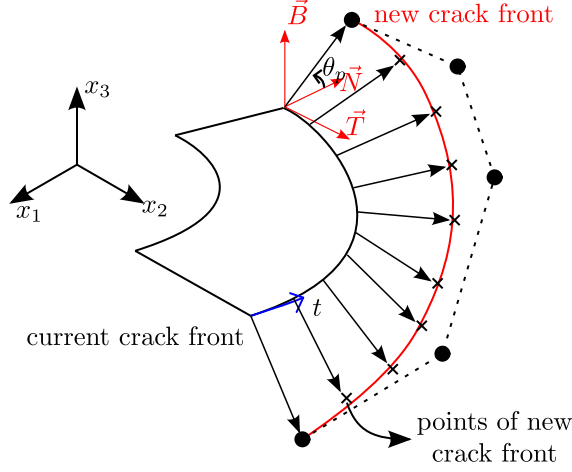


Figure 3: Definition of new crack position based on points and the corresponding new crack front.

points that defined the previous crack front so that they best fit the new crack front points. However, this strategy does not allow the NURBS weights to be adjusted during the crack growth procedure, which leads to a sub-optimal representation of the crack front during its advance. In the current work, we develop a least-squares fitting, as in [68], for the definition of the new crack front based on an isogeometric representation with NURBS curves.

The new procedure for the crack front updating using the IGABEM considers initially that the previous knot-span and degree of the NURBS crack front remains the same for the new crack front. The sample points \tilde{C}_k^{ij} define the coordinate in the k direction of the updated front, and these come from a point-wise propagation of a uniformly spaced set of points from a parametric knot u_j^i on the NURBS curve i that defines the growing crack front. The algorithm considers a crack propagation for multiple crack surfaces simultaneously. Figure 3 illustrates this sampling procedure and the definition of the new point based on Δa and θ_p .

In this strategy, the new crack front interpolation uses NURBS basis functions in its parametrisation $C_k(u_j^i, \mathbf{P}^i, \mathbf{w}^i)$ as:

$$C_k(u_j^i, \mathbf{P}^i, \mathbf{w}^i) = \sum_{j=1}^{n_P} \phi_j P_k^{ij} \quad (66)$$

in which the basis functions ϕ_j come from eq. (13) of a total of n_P basis functions, and contain the control points' weights, and P_k^{ij} is the j -th control point of the NURBS curve i in the k direction.

The least-squares fitting algorithm proceeds by writing a minimisation problem for the squared distance of the sampled point \tilde{C}_k^{ij} :

$$\min F = \mathbf{f}^T \mathbf{f} \quad (67)$$

$$f_\ell = C_k(u_j^i, \mathbf{P}^i, \mathbf{w}^i) - \tilde{C}_k^{ij} \quad (68)$$

in which \mathbf{P}^i and \mathbf{w}^i are the control points and weights of the optimised NURBS curve, and the presentation is made more compact by using $\ell \equiv ijk$ as notation for a global connectivity index related to the indices i , j , and k . These two sets of variables are the output of this analysis. By applying the Gauss-Newton method and its truncation in the first term, the eq. (67) becomes:

$$\mathbf{J}^T \mathbf{J} \Delta \mathbf{x} = -\mathbf{J}^T \mathbf{f} \quad (69)$$

in which the vector $\Delta \mathbf{x} = \{\Delta \mathbf{P} \ \Delta \mathbf{w}\}^T$ contains the increments in each of the optimising variables (control points and weights), and the Jacobian vector \mathbf{J} is:

$$\mathbf{J} = [\mathbf{J}_P \ \mathbf{J}_w] \quad (70)$$

corresponding to the first derivative of the vector \mathbf{f} with respect to \mathbf{P}^i and \mathbf{w}^i , for \mathbf{J}_P and \mathbf{J}_w , respectively. Their expressions are present in [68]. It is worth mentioning that the first and the last control points of each NURBS curve are fixed based on the propagation angle and crack increment of the end points. When a NURBS curve endpoint shares its position with an endpoint of another NURBS curve, their corresponding control point is taken as the average of the points resulting from the propagation of each patch separately, as shown in fig. 4. This guarantees a C^0 continuity when multiple NURBS surfaces, and therefore multiple NURBS curves, describe a single crack.

After finding the set of control points and weights that best approximates the new crack front, the enrichment nature requires also tangential and normal alignments between the junctions of each NURBS curve. For problems with multi-patch NURBS surfaces representing the crack surface, the optimisation for the crack growth update does not guarantee continuity for the local coordinate system at these points, which is a requirement for the set of the enrichment functions herein applied. To overcome this issue, a gradient descent algorithm promotes the alignment between the tangents and the normal outward vectors at each endpoint. The tangent vector at the end points is aligned with the vector between the first and second control points, for the initial point, or between the penultimate and last control points, for the final point, as illustrated in fig. 5.

Following the definition of fig. 5, let $\vec{A} = \mathbf{P}^A - \mathbf{P}^e$ be the vector between the endpoint \mathbf{P}^e and the point \mathbf{P}^A from the NURBS curve c_m , while $\vec{B} = \mathbf{P}^B - \mathbf{P}^e$ is

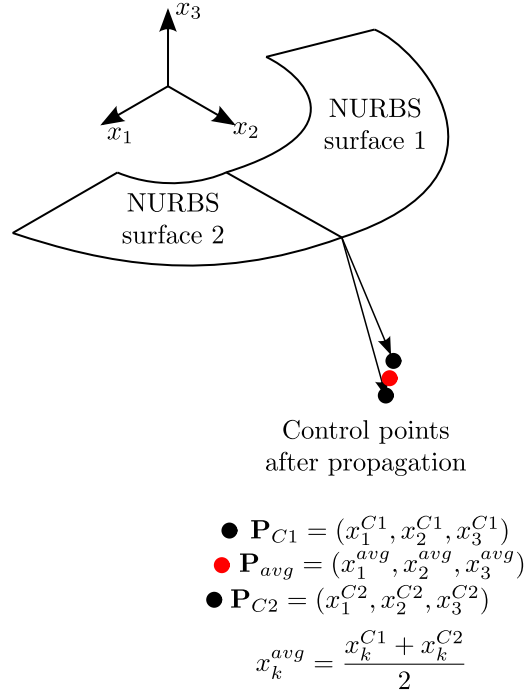


Figure 4: Averaging endpoints to guarantee C^0 continuity between NURBS surfaces.

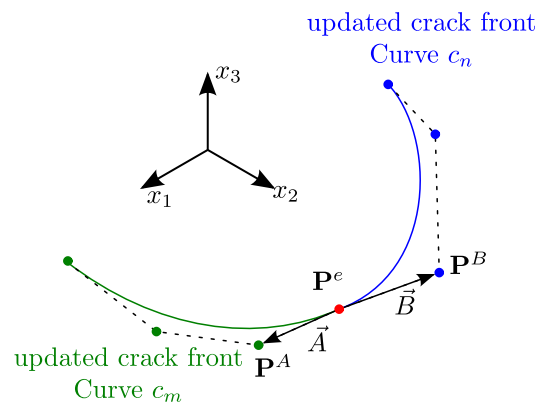


Figure 5: Control points position for each updated crack front for tangent alignment.

the vector from \mathbf{P}^e to the \mathbf{P}^B on the neighbouring NURBS curve c_n . The tangent alignment comes from a collinearity condition as:

$$g_1 = 1 - \left| \frac{\vec{A} \cdot \vec{B}}{\|\vec{A}\| \|\vec{B}\|} \right| = 0 \quad (71)$$

in which both \vec{A} and \vec{B} are functions only of the second/penultimate control points of the curves c_m and c_n . The gradient descent strategy updates the control points \mathbf{P}^A and \mathbf{P}^B as:

$$\begin{Bmatrix} \mathbf{P}^A \\ \mathbf{P}^B \end{Bmatrix}^{k+1} = \begin{Bmatrix} \mathbf{P}^A \\ \mathbf{P}^B \end{Bmatrix}^k - \alpha_{GD} \begin{Bmatrix} \frac{\partial g_1}{\partial \mathbf{P}^A} \\ \frac{\partial g_1}{\partial \mathbf{P}^B} \end{Bmatrix}^k \quad (72)$$

in which the partial derivatives are:

$$\frac{\partial g_1}{\partial P_\ell^A} = - \frac{\text{sign}(\vec{A} \cdot \vec{B}) B_\ell \|\vec{A}\| \|\vec{B}\| - \frac{(\vec{A} \cdot \vec{B})(P_\ell^A - P_\ell^e) \|\vec{B}\|}{\|\vec{A}\|}}{(\|\vec{A}\| \|\vec{B}\|)^2} \quad (73)$$

$$\frac{\partial g_1}{\partial P_\ell^B} = - \frac{\text{sign}(\vec{A} \cdot \vec{B}) A_\ell \|\vec{A}\| \|\vec{B}\| - \frac{(\vec{A} \cdot \vec{B})(P_\ell^B - P_\ell^e) \|\vec{A}\|}{\|\vec{B}\|}}{(\|\vec{A}\| \|\vec{B}\|)^2} \quad (74)$$

In the incremental procedure, the stopping criterion is based on the scalar g_1 associated to the tangent alignment condition. α_{GD} is a parameter set in the beginning of the analysis that considers the influence of the gradient during the iterative process. The alignment conditions are applied sequentially, in which firstly the tangent alignment occurs, and its result is the input data for the normal alignment. The normal outward alignment condition stems from using the inner product of the normal outward vector from each neighbouring NURBS curve as:

$$g_2 = 1 - |\vec{N}^m \cdot \vec{N}^n| = 0 \quad (75)$$

in which \vec{N}^m and \vec{N}^n are the normal vectors at the shared point of the curves c_m and c_n . The gradient descent method for the outward normal vectors occurs in a similar fashion as eq. (72), but updating all control points of each NURBS curve

$$\begin{Bmatrix} \mathbf{P}^m \\ \mathbf{P}^n \end{Bmatrix}^{k+1} = \begin{Bmatrix} \mathbf{P}^m \\ \mathbf{P}^n \end{Bmatrix}^k - \alpha_{GD} \begin{Bmatrix} \frac{\partial g_2}{\partial \mathbf{P}^m} \\ \frac{\partial g_2}{\partial \mathbf{P}^n} \end{Bmatrix}^k \quad (76)$$

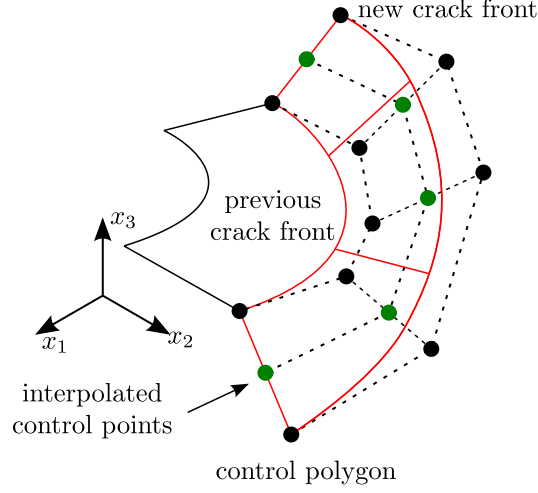


Figure 6: New crack surface generation based on new crack front.

and the partial derivatives associated to the normal outward alignment are:

$$\frac{\partial g_2}{\partial P_\ell^m} = \text{sign}(g_2) \sum_{k=1}^3 \left(\frac{\partial N_k^m}{\partial P_\ell^m} N_k^n \right) \quad (77)$$

$$\frac{\partial g_2}{\partial P_\ell^n} = \text{sign}(g_2) \sum_{k=1}^3 \left(\frac{\partial N_k^n}{\partial P_\ell^n} N_k^n \right) \quad (78)$$

in which a finite difference strategy computes the partial derivatives of the normal outward vector due to their complex analytical determination.

4.2. Modifications in the XIGABEM algebraic system

The fatigue crack propagation analysis with XIGABEM requires an incremental simulation, in which for each propagation step a new set of isogeometric surfaces represents the updated crack front. The generation of these new crack surfaces relies on the connection between the previous and the updated crack front as illustrated in fig. 6. The perpendicular direction receives the same knot vector as the previous surface. The new control points of this surface are found from a direct interpolation between the control points of the previous and new fronts.

The Greville Abscissae strategy generates the collocation points on the new surfaces, and application of the relevant boundary integral equations at these points requires integration over all the existing domain. In addition, the integration over the new portion of the boundary, formed by the latest crack surface increment(s), is also required for the pre-existing collocation points. In this stage, additional rows

and columns arise in the algebraic system, the rows referring to the new collocation points and the columns to the displacement and traction coefficients for the new surfaces. It is important to recall that the remainder of the algebraic system is unaffected by the introduction of new crack surface elements.

After the definition of the new crack front, the determination of the enrichment terms occurs simultaneously to the integration of the corresponding new surfaces. With the definition of the new crack front, all enrichment terms from the previous step are removed from the system, and previously enriched elements return to the standard (unenriched) IGABEM description.

5. Numerical applications

5.1. Elliptical crack growth

The first application of this study involves the fatigue analysis of an elliptical shaped crack immersed in a prismatic solid. The geometry and boundary conditions are presented in fig. 7, in which the crack centre is at the coordinates (0,0,0). A uniformly distributed traction varying from $\sigma_2^{min} = 0\text{MPa}$ to $\sigma_2^{max} = 200\text{MPa}$ is applied on the upper face, while the lower face is clamped. The material is a Ti-6Al-4V alloy, whose properties are given in section 5.1. The Paris constants provided assume units of ΔK and da/dN to be $\text{MPa mm}^{0.5}$ and mm/cycle . The numerical modelling of the elliptical crack considers 5 bi-quadratic ($p = q = 2$) NURBS surfaces modelling each crack surface, as in fig. 13, i.e. 10 NURBS surfaces are used for both crack sides. The inner elliptical surface has dimensions equivalent to 80% of the elliptical crack. The complex K_I variation along the crack front affects the crack propagation increment by triggering eq. (56). This application has been studied by Ilie and Ince [69], in which a finite element analysis obtained results that approximate well their proposed reference solution for the crack front advancement. The fatigue analysis stops after 10 increments.

Young Modulus	$E = 115\text{GPa}$
Poisson's ratio	$\nu = 0.3$
Paris constant	$C = 1.77 \cdot 10^{-14}$
Paris exponent	$m = 3.667$
Maximum increment	$\Delta a_{max} = 0.6\text{mm}$

Table 1: Material and fatigue properties of Ti-6Al-4V alloy.

Three isogeometric meshes are used to test the performance of the proposed XIGABEM algorithm for the propagation of the elliptical crack under the given

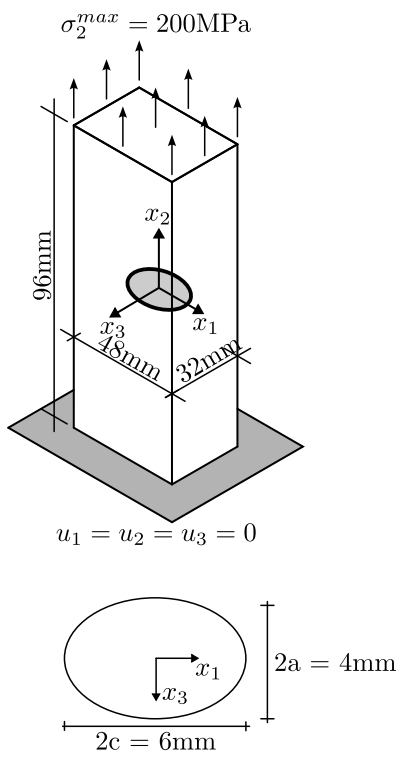


Figure 7: Geometry and boundary conditions of elliptical crack immersed in prismatic solid.

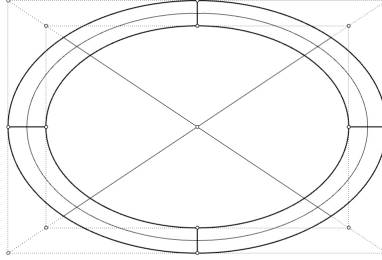


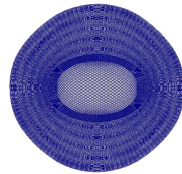
Figure 8: Isogeometric mesh and control points for elliptical crack.

cyclical load. The coarse mesh, namely mesh 1 and shown in fig. 8, has its control points, weights and knot-vectors given in the Appendix A. The uniform knot insertion refinement in both directions of mesh 1 generates the finer meshes 2 and 3. Meshes 1, 2 and 3 have 114, 184 and 274 collocation points, respectively, for the initial crack. The Schollmann criterion is adopted for the determination of the crack propagation angle; however, since the in-plane elliptical crack has a pure mode I response, there is no significant difference between the two criteria used in this study. In addition, table 2 presents the number of degrees of freedom in each propagation step, which highlights the XIGABEM ability of representing a curved problem with a small number of degrees of freedom.

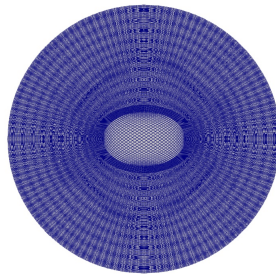
The crack configuration for Mesh 2, in the first step, the fifth step and the last step, are shown in fig. 9. In addition, fig. 10 presents the deformed shape amplified by a factor of 1000 for each mesh in their last propagation step. As expected for this geometry during crack growth, the crack geometry transforms from its initial elliptical shape into a circular shape. Additionally, the XIGABEM formulation promotes the tying between the upper and lower crack faces for the last increment, and this reduces the error in this region. Also, all three meshes give rise to a similar displacement field, which demonstrates the ability of the XIGABEM formulation to capture the response well even using coarse meshes. Moreover, the fatigue life cycle assessment for the elliptical crack in fig. 11 demonstrates a convergence pattern for the required amount of cycles, and this response agrees with the reference solution of Ilie and Ince [69].



Step 1



Step 5



Step 10

Figure 9: Elliptical crack growth: steps 1, 5 and 10.

step	Number of degrees of freedom		
	Mesh 1	Mesh 2	Mesh 3
0	378	600	882
1	594	888	1362
2	810	1176	1842
3	1026	1464	2322
4	1242	1752	2802
5	1458	2040	3282
6	1674	2328	3762
7	1890	2616	4242
8	2106	2904	4722
9	2322	3192	5202
10	2538	3480	5682

Table 2: Number of degrees of freedom at each propagation step

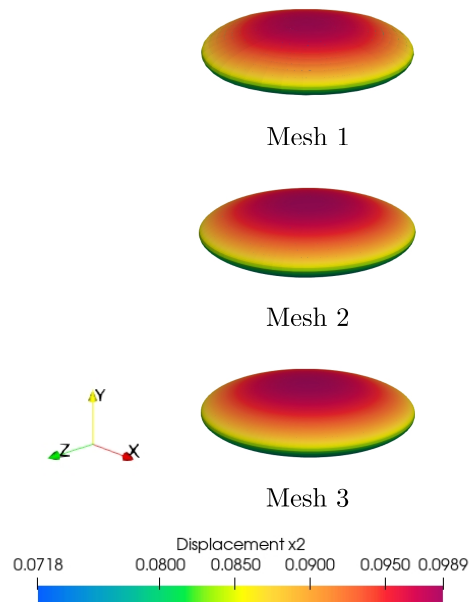


Figure 10: Deformed shape for each mesh in tenth propagation step.

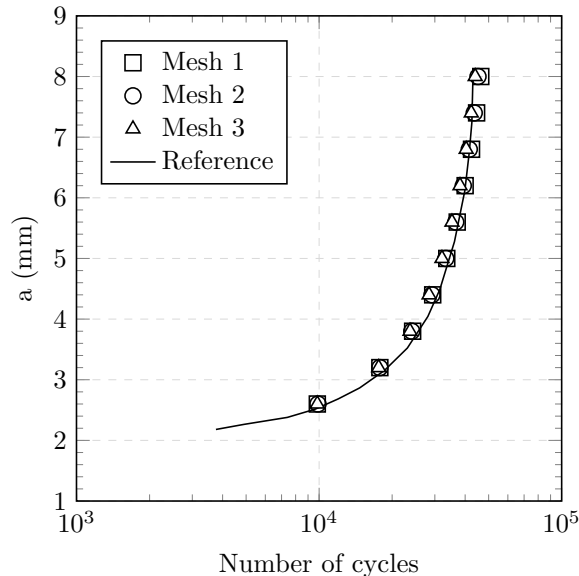


Figure 11: Fatigue life assessment of elliptical crack in in prismatic solid.

5.2. Inclined penny-shaped crack growth

The second numerical application of this study consists of an inclined penny-shaped crack as shown in fig. 12. The crack has radius $R = 0.1\text{m}$, is located centrally in a cube of side $a = 2.0\text{m}$, and is inclined by an angle $\pi/4$ rad. The isogeometric mesh for the crack geometry contains 5 NURBS surfaces of degree $p = q = 2$ for each crack surface, i.e. a total of 10 NURBS surfaces is used for the crack. The central portion of the crack is circular with a radius $R_{int} = 0.08\text{m}$ while the annular outer portion of the crack is modelled using 4 NURBS surfaces, as shown in fig. 13. For the numerical analysis, this geometrical mesh undergoes two knot insertions in each parametric direction, which results in a total of 274 collocation points. In the face in which $x_1 = -1.0$, the prescribed displacement is $u_1 = 0.0$, while lower face $x_2 = -1.0$ has $u_2 = 0.0$ and the face with $x_3 = -1.0$ contains $u_3 = 0.0$ as an enforced displacement. The upper face $x_2 = 1.0$ is subjected to a load varying cyclically between $\sigma_2^{min} = 0\text{MPa}$ and $\sigma_2^{max} = 1\text{MPa}$. Continuity is not enforced between each crack surface, which justifies the local adjustment for tangent and normal outward vectors. The loading condition results in a fully mixed mode I/II/III response due to the crack inclination. Pereira et al. [17] analysed this geometry with the hp-generalised FEM approach, in which the Schollmann criterion defined the crack growth direction for the crack. The material and fatigue properties are presented in section 5.2, in which the Paris constants assumed the units used for ΔK and da/dN to be $\text{MPa mm}^{0.5}$ and mm/cycle . The fatigue

analysis terminates after 20 propagation steps. The proportion between the initial crack and the final crack configuration from the results obtained by Pereira et al. [17] indicates that those authors applied a Δa_{\max} of 0.1m rather than the value of 0.002m stated in their description. Our parameters adopted in this study are tuned to allow a direct comparison of the end state of the crack against the Pereira et al. [17] results. The hoop stress criterion and the Schollmann criterion are both tested for defining the crack evolution. In addition, these two criteria are compared using K_{III} in their equations (as expected) and taking $K_{III} = 0$ for the crack propagation angle and equivalent SIF, in an attempt to compare with Pereira et al. [17]. This application has a reference solution [70] for the LEFM case of the inclined penny-shaped crack in its initial configuration that considers an infinite block subjected to an uniform tensile loading, being:

$$K_I = \frac{2\sigma_0}{\pi} \sqrt{\pi R} \cos^2 \theta_c \quad (79)$$

$$K_{II} = \frac{4\sigma_0}{\pi(2-\nu)} \sqrt{\pi R} \cos \theta_i \sin \theta_i \cos \theta_f \quad (80)$$

$$K_{III} = \frac{4\sigma_0(1-\nu)}{\pi(2-\nu)} \sqrt{\pi R} \cos \theta_i \sin \theta_i \sin \theta_f \quad (81)$$

in which θ_f corresponds to the angle along the crack front and θ_i is the inclination angle in the x_2x_3 plane between the x_3 axis and the radius.

Young Modulus	$E = 1000\text{MPa}$
Poisson's ratio	$\nu = 0.3$
Paris constant	$C = 1.5463 \cdot 10^{-11}$
Paris exponent	$m = 2.1$
Maximum increment	$\Delta a_{\max} = 0.0185\text{m}$

Table 3: Material and fatigue properties of inclined penny-shaped crack.

The crack configurations for the initial geometry, and for the seventh, fourteenth and twentieth steps are presented in fig. 14, considering both hoop stress and Schollmann criteria and the presence or absence of K_{III} in the propagation analysis. Figure 15 shows the final crack configuration reproduced from Pereira et al. [17]. Both geometries are similar when comparing all four scenarios obtained by XIGABEM with the reference response with the Schollmann criterion. As expected, the crack grows in a manner leading towards a pure mode I configuration with the Schollmann criterion, as also found in the reference solution. However, the hoop stress criterion with and without K_{III} influence and the Schollmann criterion without K_{III} also lead to a similar crack configuration to that predicted using

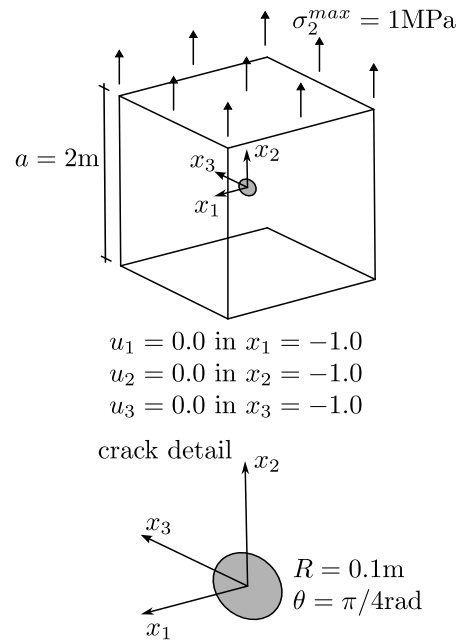


Figure 12: Geometry and boundary conditions of inclined penny-shaped crack.

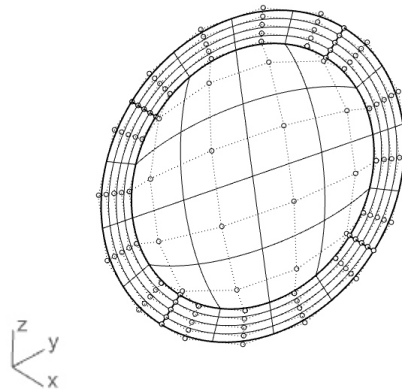


Figure 13: Isogeometric mesh and control points position for inclined penny-shaped crack.

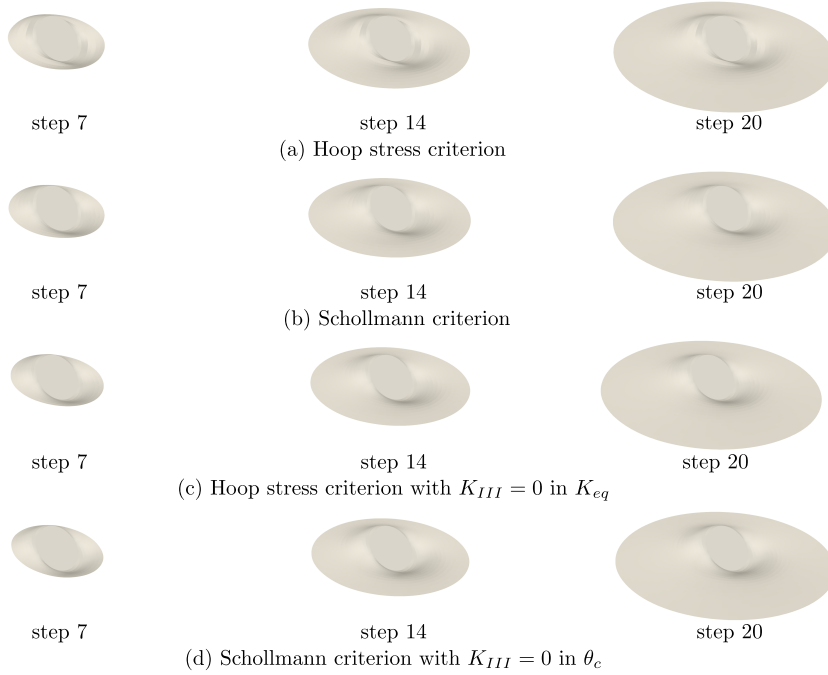
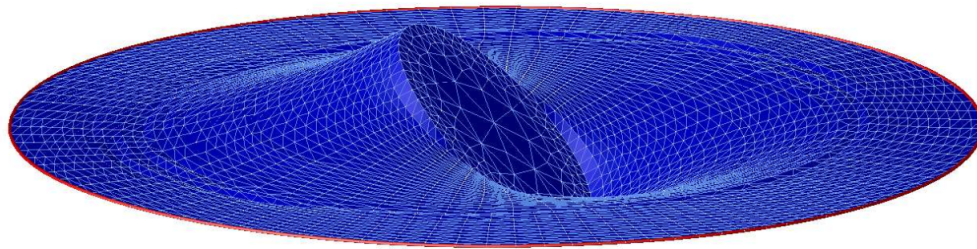


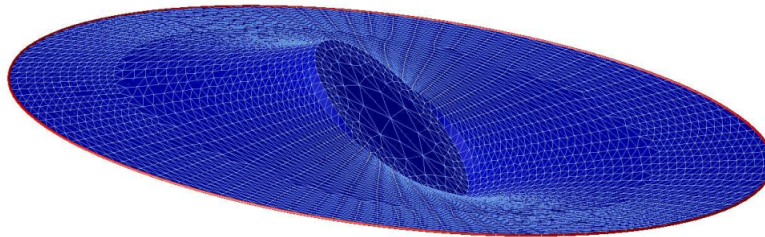
Figure 14: Inclined penny-shaped crack configuration during fatigue growth by XIGABEM considering (a) Hoop stress criterion, (b) Schollmann criterion, (c) Hoop stress criterion with $K_{III} = 0$, and (d) Schollmann criterion with $K_{III} = 0$.

the Schollmann criterion considering K_{III} effects. This suggests that the choice between these two criteria for this application does not significantly alter the final response. This contrasts with Pereira et al. [17], who found their crack configuration when $K_{III} = 0$ not to reach a fully in-plane, circular geometry at the end of the analysis; the XIGABEM response is similar for all four different scenarios in the present study. In addition, the number of degrees of freedom at the last propagation step for the XIGABEM response is 8082, demonstrating the ability of XIGABEM to obtain accurate solutions for cracked problems with a small number of degrees of freedom.

The SIF comparison between the results obtained by the XIGABEM and the solution from Pereira et al. [17] for the final propagation step and using the Schollmann criterion is shown in fig. 16. In addition, the average value for K_I and the coefficient of variation (standard deviation divided by the mean value) for each case and the Pereira et al. [17] solution in its last propagation step are presented in table 4. The discrepancy between the results and the reference solution may be associated to the absence of the crack front torsion angle in the definition of the



(a) Schollmann criterion - hp-GFEM



(b) Schollmann criterion with $K_{III} = 0$ - hp-GFEM

Figure 15: Inclined penny-shaped crack configuration from the hp-GFEM approach [17], considering (a) Schollmann criterion and (b) Schollmann criterion with $K_{III} = 0$.

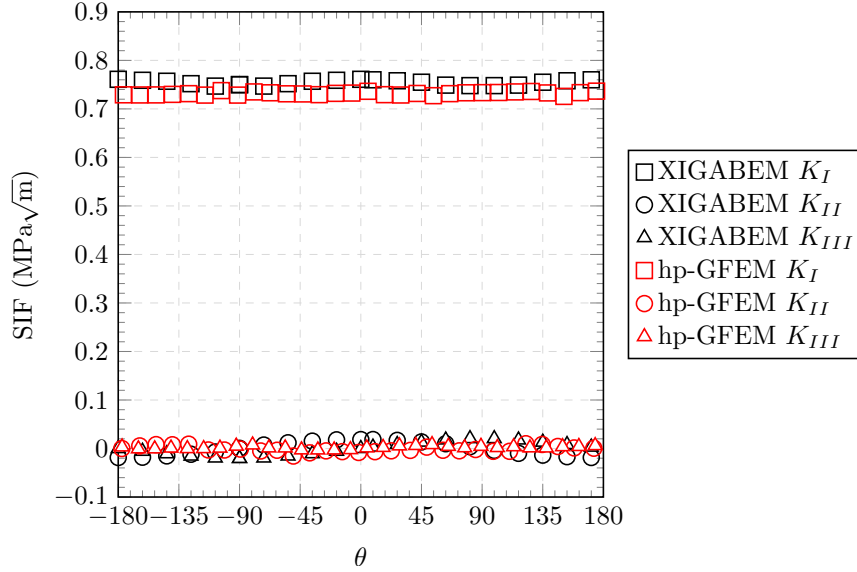


Figure 16: SIF distribution along crack front at the last propagation step: Schollmann criterion and comparison against hp-GFEM results from Pereira et al. [17].

new crack front in comparison to the hp-GFEM approach. Still, both strategies result in approximately constant K_I along the crack front, which is further evidence that the crack has evolved to a circular shape in a plane perpendicular to the applied load. In addition, the K_{II} and K_{III} values have reduced to negligible values by the last propagation step.

Figure 17 compares the SIFs between the XIGABEM approach and the hp-GFEM approach [17] with the Schollmann criterion using $K_{III} = 0$ during propagation, and for the last propagation step. The most important result for this problem, i.e. K_I , is largely unaffected by taking $K_{III} = 0$. The XIGABEM results for K_{II} and K_{III} are also very similar to the case in which K_{III} is not taken to be zero for the calculation of the propagation angle. Accordingly, the XIGABEM formulation was capable of achieving a pure mode I response, while the oscillation in the hp-GFEM results of Pereira et al. [17] is consistent with the final geometry of the crack not having reached a plane perpendicular to the applied load. Also, fig. 18 presents the SIFs for the last step using the hoop stress criterion, with K_{III} and without K_{III} effects on the equivalent SIF, respectively. Similarly, in these two cases, the SIF distribution matches that found with the Schollmann criterion (both with and without K_{III} effects on the propagation angle), which indicates that for the XIGABEM formulation the adoption of either of these two criteria will lead to similar responses.

	avg. K_I (MPa \sqrt{m})	Coefficient of Variation
Pereira et al. [17]	0.7316	0.40%
Hoop stress criterion	0.7511	0.84%
Schollmann criterion	0.7541	0.66%
Hoop stress criterion $K_{III} = 0$ in K_{eq}	0.7505	0.41%
Schollmann criterion $K_{III} = 0$ in θ_c	0.7491	0.38%

Table 4: Average values for K_I in the last propagation step for Hoop stress criterion and for Schollmann criterion.

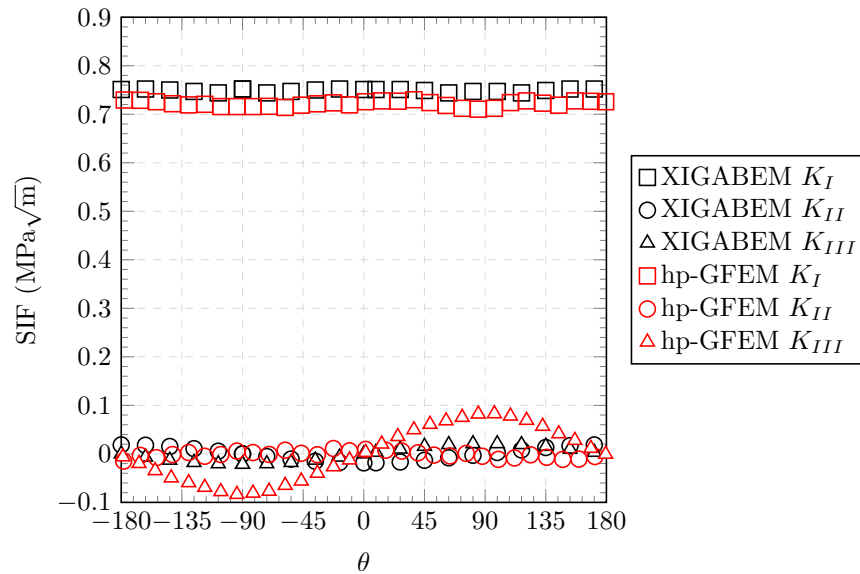


Figure 17: SIF distribution along crack front at the last propagation step: Schollmann criterion considering $K_{III} = 0$ for propagation angle and comparison against hp-GFEM results from Pereira et al. [17].

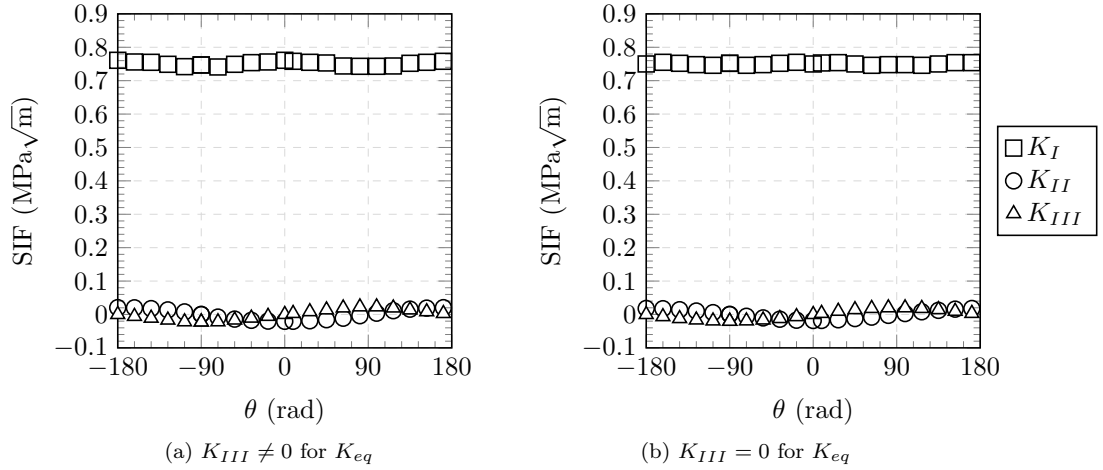


Figure 18: SIF distribution along crack front at the last propagation step with the hoop stress criterion and the influence of K_{III} in the equivalent SIF.

Figure 19, fig. 20 and fig. 21 present the evolution of each SIF during propagation using the hoop stress criterion, while fig. 22, fig. 23 and fig. 24 correspond to the SIF evolution using the Schollmann criterion. Additionally, these graphs present the SIF variation of the initial configuration (step 0) along the crack front and its comparison with the reference solution given by eq. (79), eq. (80), and eq. (81). Based on the comparison for the initial geometry, the XIGABEM response agrees with the reference response, as also previously found by Rocha et al. [47] for a crack with different dimensions. In addition, the SIF evolution is of great interest for the scientific community as it provides benchmark responses. Based on their evolution, it is evident that the pure mode I behaviour, in which the crack has evolved to lie in a plane perpendicular to the applied load, has developed by step 14, since K_{II} and K_{III} have reduced to values close to zero in this step; they do not reduce further from step 14 to step 20. The crack configuration in fig. 14 justifies this claim, due to the planar circular shape the crack assumes in the step 14.

Furthermore, fig. 25 presents the required number of cycles for the crack growth for all four analysed cases. For the initial steps, there is a noticeable difference in the required number of cycles for a given increment for each criterion. This effect tends to reduce throughout the analysis, in the same pace as the crack pursues a pure mode I response. At the final stages, all four analysis strategies predict similar numbers of cycles, which is consistent with the similarity in the SIF distribution during crack propagation. This is a key result for the engineering community in that users of this numerical method do not need to be overly concerned about

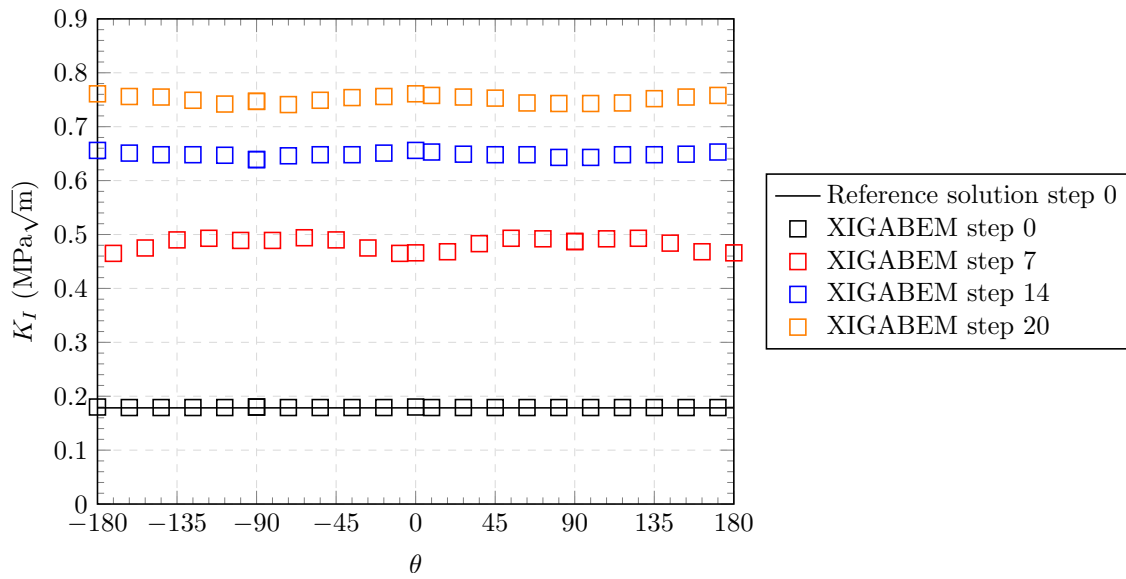


Figure 19: K_I distribution along crack front at steps 0, 7 and 14 for hoop stress criterion.

choice between the hoop stress and Schollmann criteria, nor the choice of how to deal with K_{III} in propagating the crack, since the discrepancies in the main result they seek (the fatigue life) are smaller than the margin for error engineers would apply in these circumstances.

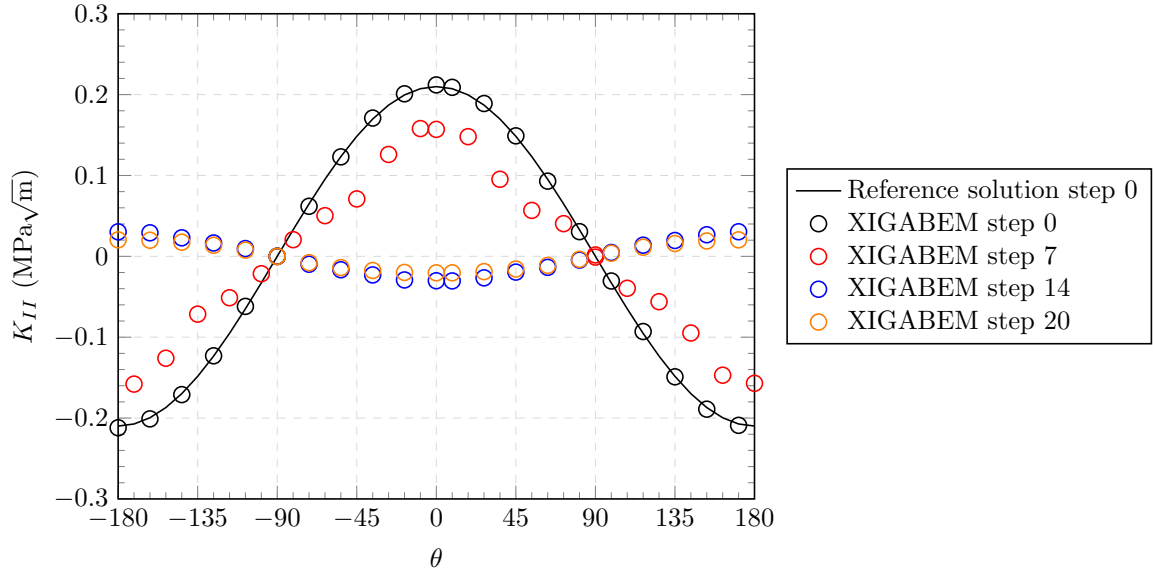


Figure 20: K_{II} distribution along crack front at steps 0, 7 and 14 for hoop stress criterion.

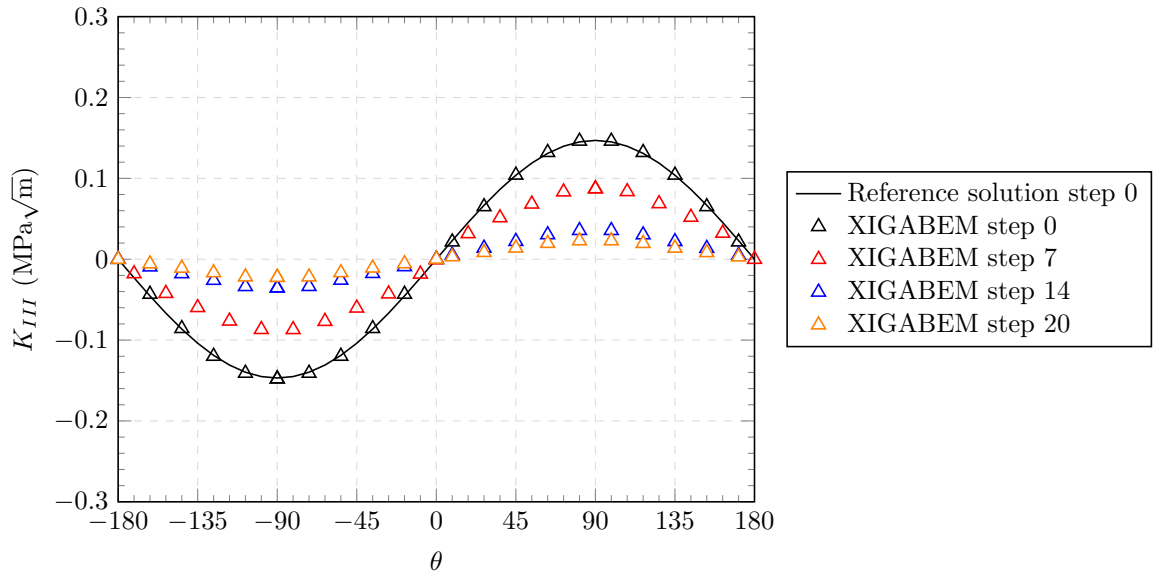


Figure 21: K_{III} distribution along crack front at steps 0, 7 and 14 for hoop stress criterion.

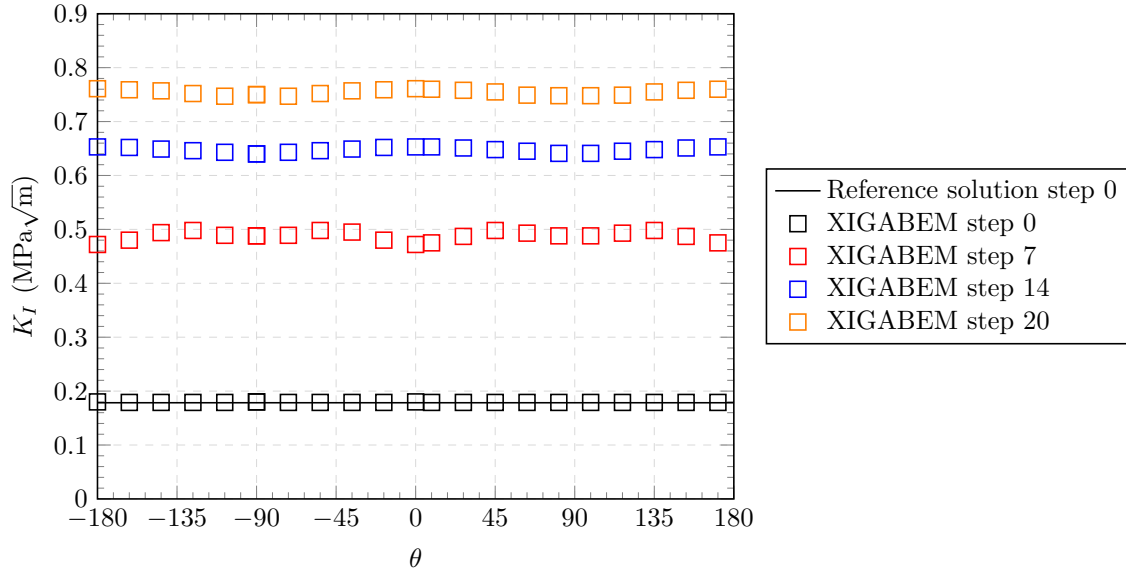


Figure 22: K_I distribution along crack front at steps 0, 7 and 14 for Schollmann criterion.

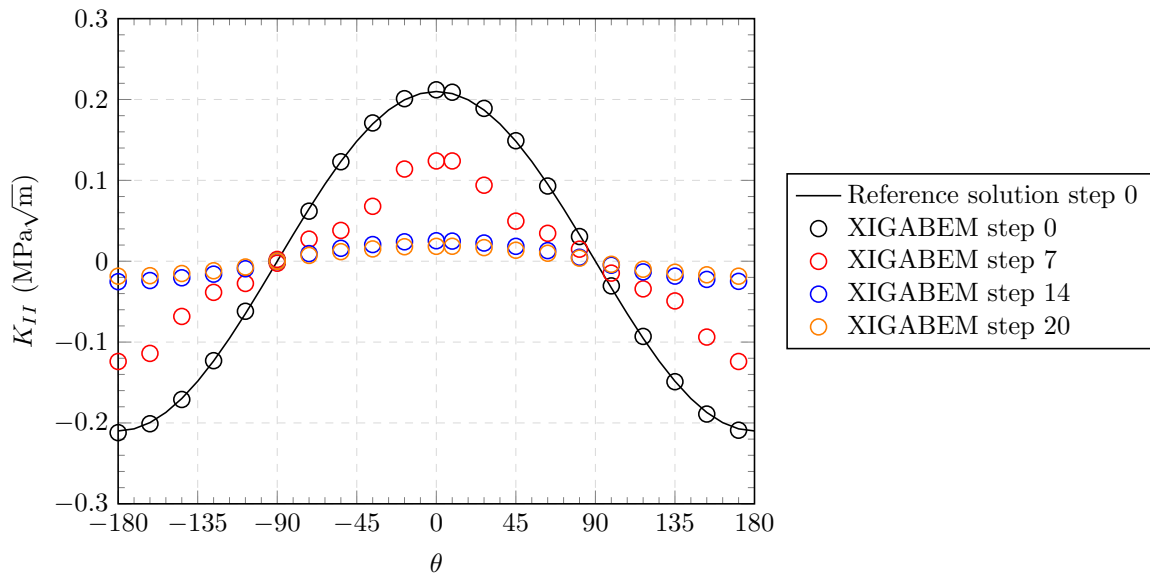


Figure 23: K_{II} distribution along crack front at steps 0, 7 and 14 for Schollmann criterion.

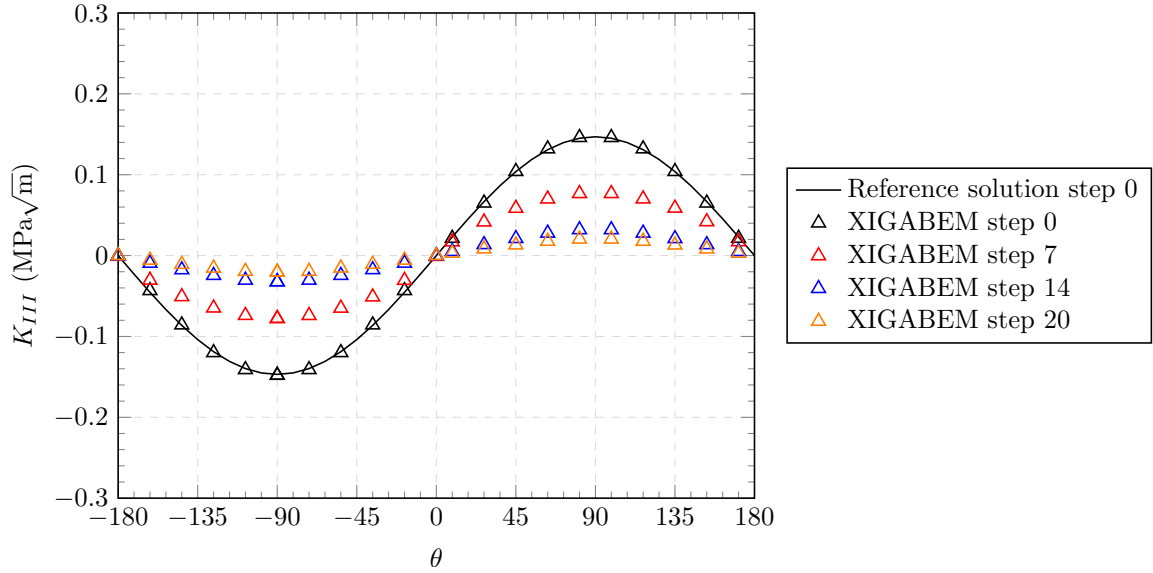


Figure 24: K_{III} distribution along crack front at steps 0, 7 and 14 for Schollmann criterion.

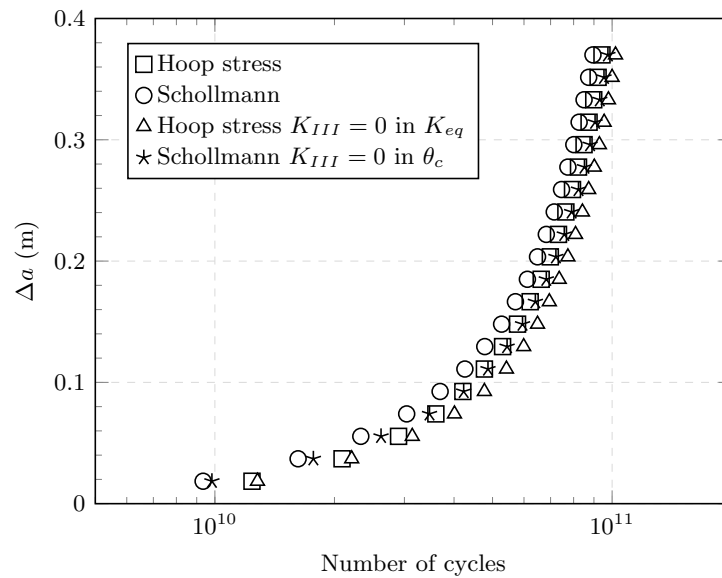


Figure 25: Fatigue life assessment of inclined penny-shaped crack.

5.3. Hook under cyclic loading

The third application of this study involves the fatigue analysis of a hook under loading service with an initial crack near its threaded notch. The geometry presented in fig. 26 contains various curved surfaces, which suggests an isogeometric three-dimensional formulation would be appropriate to analyse this problem efficiently. The notched region is common in crane hooks, and it normally induces stress concentration regions that become fatigue crack initiation sites. This behaviour aligns with the experimental results of fatigue propagation in a crane hook as studied by Kishore et al. [71] and shown in fig. 27. A uniformly distributed traction of $t_1^{\min} = 0.0$ and $t_1^{\max} = -8.0$ kN/cm² is applied to the grey region in fig. 26, which simulates the service loading of this hook, while the surface at $x_1 = 5.0$ cm has all displacements clamped. The material properties are $E = 20,000.00$ kN/cm² and $\nu = 0.27$ for the Young's modulus and Poisson ratio, and the fatigue properties are $C = 4.10^{-12}$ and $m = 2.7$. The units of the Paris constants consider ΔK and da/dN in kPa cm^{0.5} and cm/cycle. The fatigue analysis comprises 9 propagation steps and a $\Delta a_{\max} = 0.2$ cm. The crack propagation follows the maximum hoop stress criterion. This application serves as a benchmark for the capability of the proposed formulation to represent real, complex-shaped geometries.

The isogeometric model shown in fig. 28(a) has 38 NURBS surfaces of degree $p = q = 2$ defining the external boundary, while fig. 28(b) illustrates the crack description with four NURBS surfaces of $p = q = 2$, each modelling one side of the crack. The control points, weights, connectivity, and knot vectors are provided in the supplementary material. The resulting IGABEM model undergoes two uniform knot insertions in both parametric directions on the notch and crack surfaces, resulting in a model with 738 collocation points, as shown in fig. 29.

Figure 30 presents the deformed shape of the hook under its maximum loading, considering different propagation steps and magnified 20 times. Step 0 represents the initial crack configuration. The displaced shape aligns with the expected behaviour for this geometry, which exhibits combined bending and tension. Additionally, the detailed view of the cracked region, with displacement magnified 100 times, demonstrates a smooth field along the crack surfaces. A gap in the external boundary mesh is evident at the intersection of this boundary with the crack front. This is expected, as this region is modelled using two independent, unenriched NURBS surfaces, with C^{-1} continuity between them. This gap is expected to have only a mild effect on the accuracy at the crack front since the enriched crack surfaces are responsible for SIF computation. In fig. 31, the crack front is seen to propagate faster at the edges than at its center, resulting in curvature loss during crack growth. The SIF distribution shown in fig. 32 for steps 0, 3, 6, and 9 indicates a dominant Mode I behaviour in this application. In addition, the higher values of K_I near the edges explain the faster crack growth in these regions com-

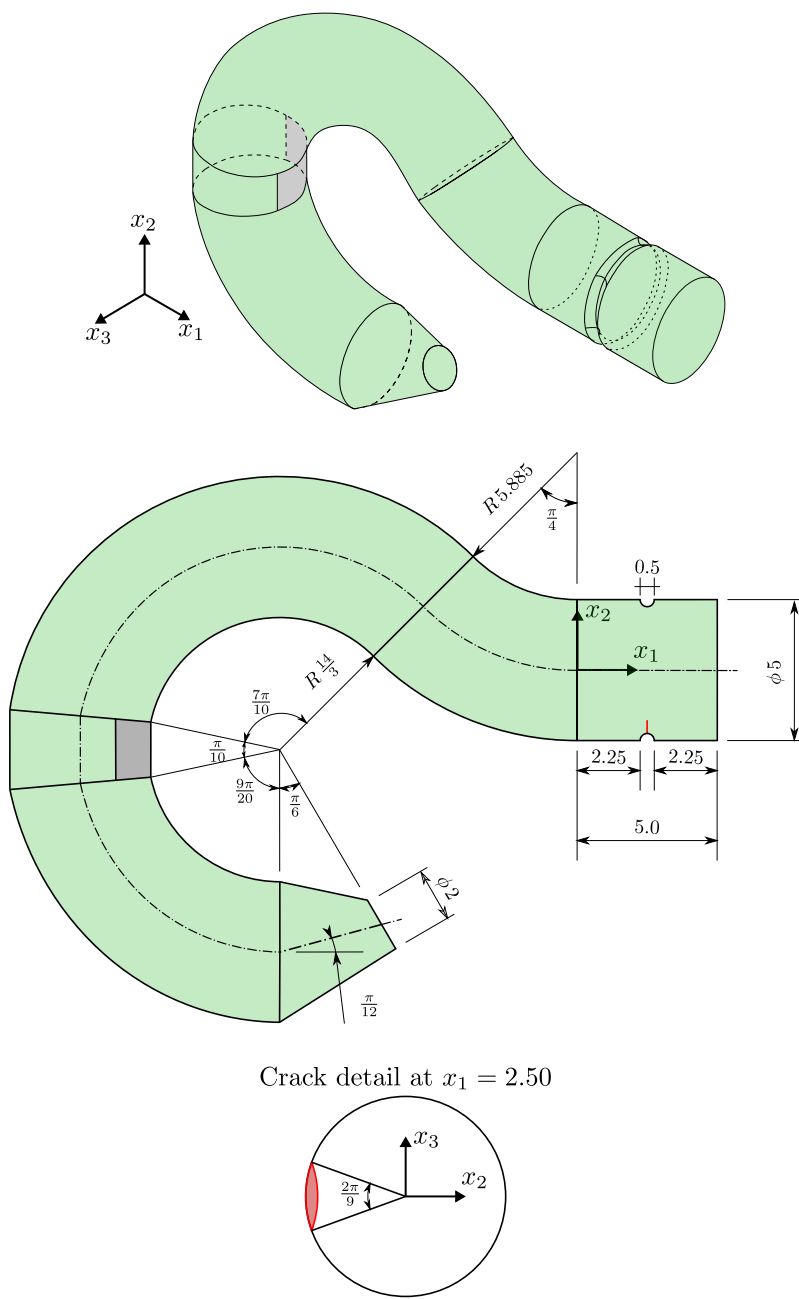
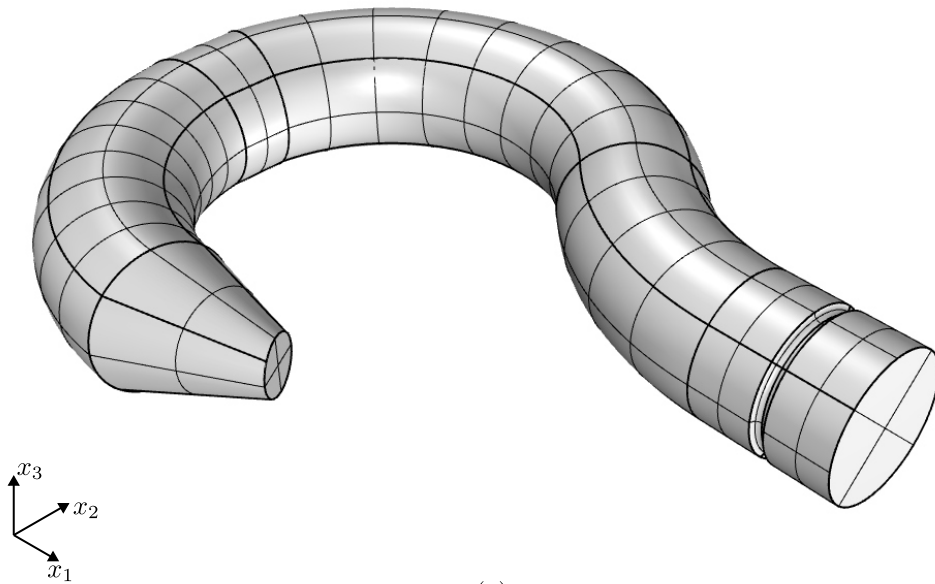


Figure 26: Geometry of hook with initial crack, dimensions in cm.

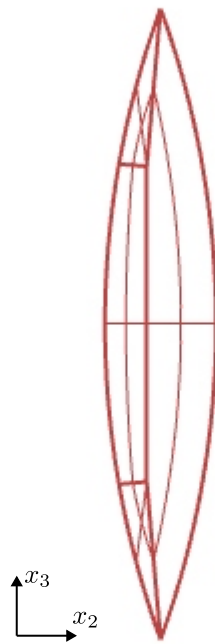


Figure 27: Fatigue crack location in crane hook experiment [71].

pared to the middle of the crack front. At later propagation steps, K_I becomes more uniform along the front, however with higher values close to the edges. Finally, fig. 34 presents the fatigue life assessment of the hook under cyclic loading as a benchmark result for the literature. In summary, the XIGABEM formulation directly captures the SIFs, even for a complex geometry involving both the external boundary and the crack, and successfully analyses an industrial configuration.



(a)



(b)

Figure 28: Isogeometric model of hook with crack.



Figure 29: Collocation points position for the XIGABEM model of hook with crack.

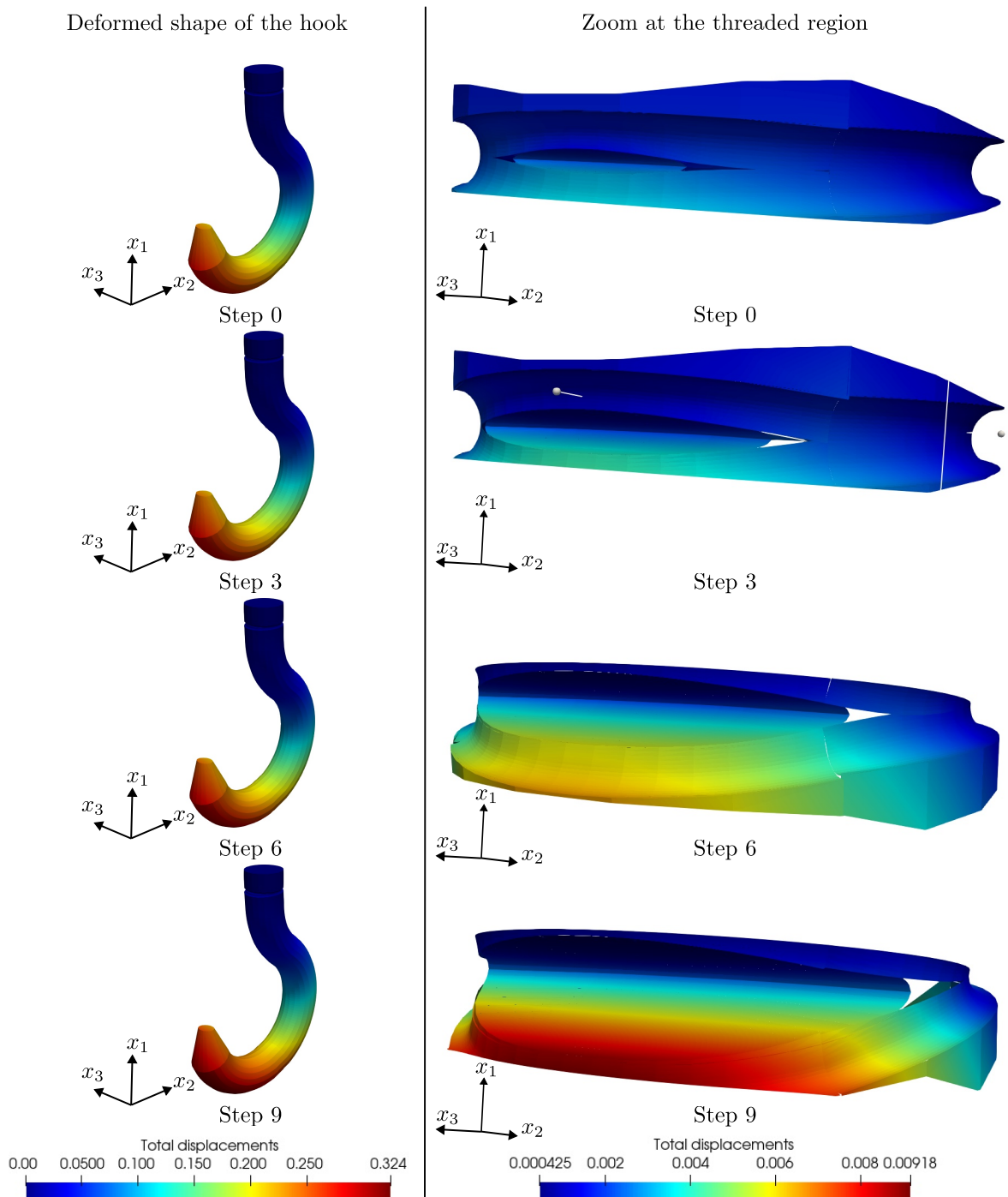


Figure 30: Deformed shape of a crane hook under cyclic loading when the load reaches its maximum value for different crack steps.

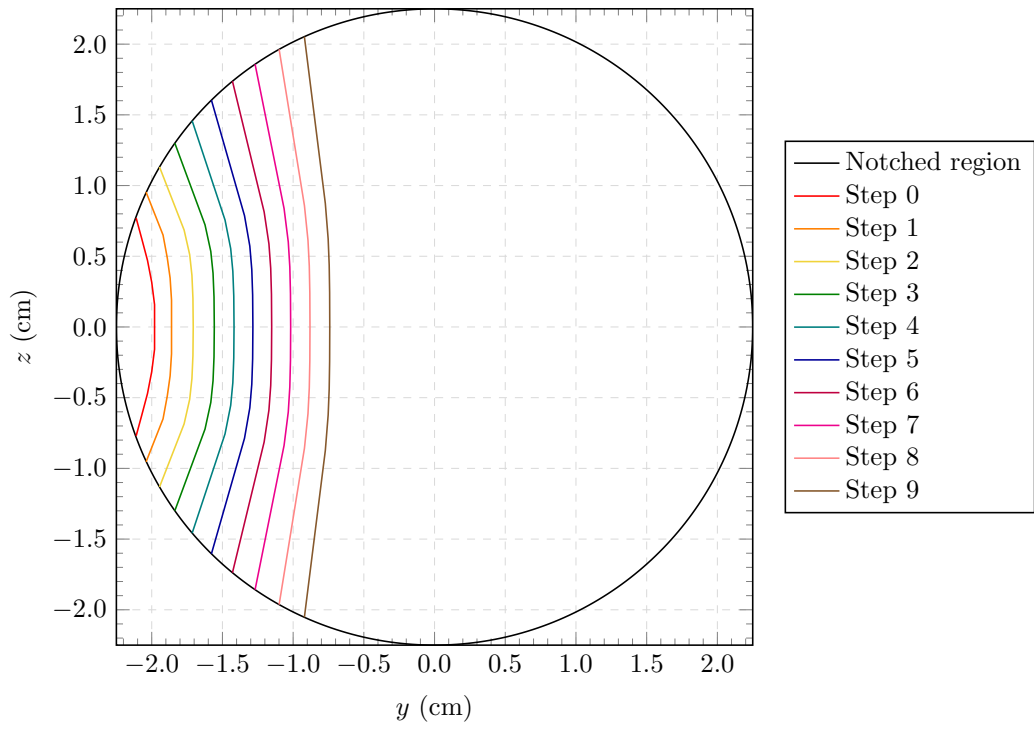
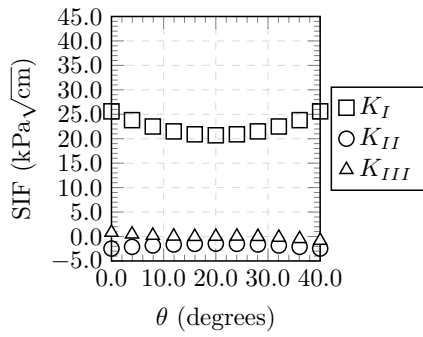
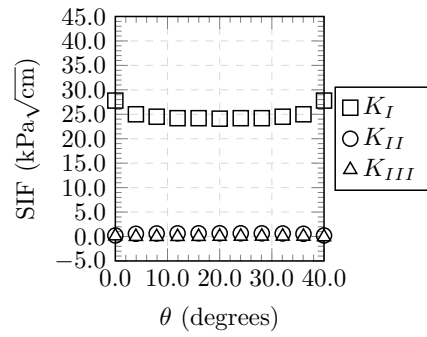


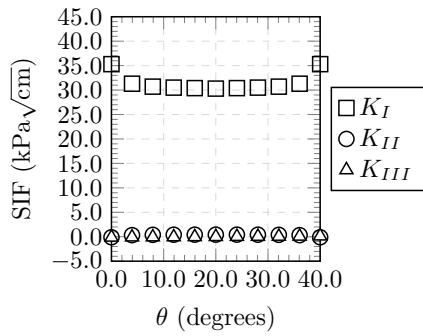
Figure 31: Crack front evolution at the plane $x_1 = 2.5$ due to the cyclic loading on the hook.



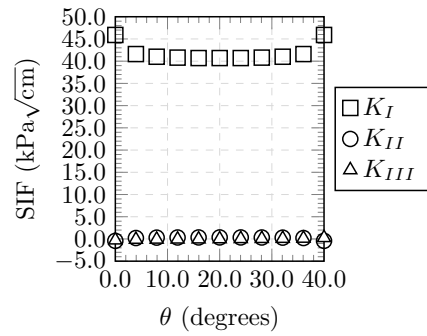
(a) Step 0



(b) Step 3



(c) Step 6



(d) Step 9

Figure 32: Stress Intensity Factors' distribution along crack front during fatigue propagation on hook.

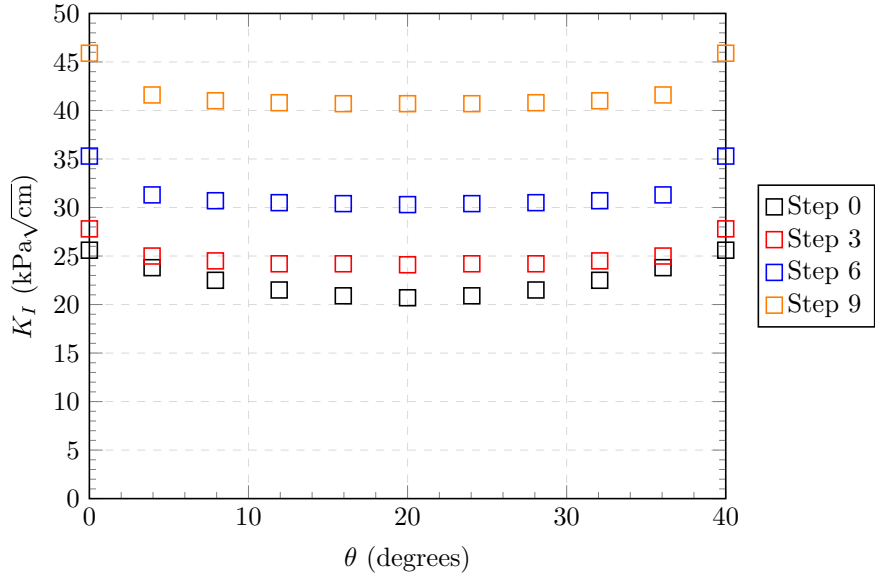


Figure 33: Evolution of K_I during fatigue propagation of a at the threaded region of a hook.

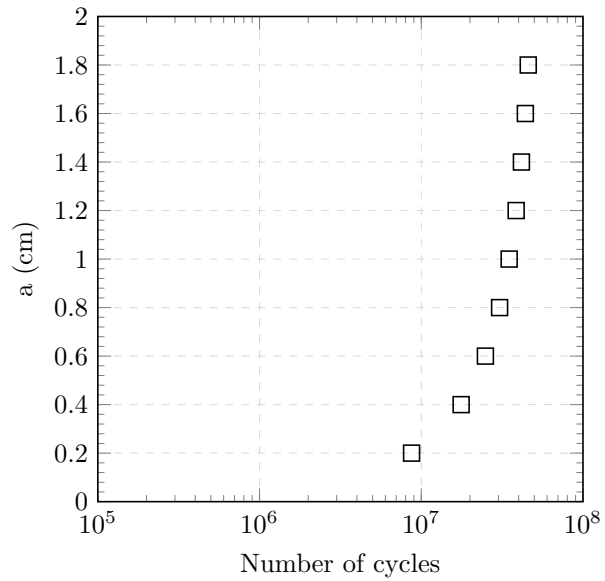


Figure 34: Fatigue life assessment of hook under cyclic loading.

6. Concluding remarks

This study presents the high-cycle fatigue modelling of three-dimensional crack configurations with the eXtended Isogeometric Boundary Element Method (XIGABEM). This formulation allows for the fatigue assessment of complex crack geometries, in which use of isogeometric basis functions is made for their accurate representation during propagation. In addition, the enrichment strategy gives rise to several advantages for the efficient determination of the mechanical solution throughout the incremental analysis with a small number of degrees of freedom.

The three-dimensional XIGABEM formulation of this study relies on the Williams-based enrichment strategy. The enrichment functions introduce interpolation parameters that allow for the direct and accurate determination of the Stress Intensity Factors, which precludes the need for computationally demanding post-processing tasks such as the J-integral or M-integral. Two crack growth criteria define the direction in which the crack advances: the hoop stress criterion and the Schollmann criterion. While the former has been applied in several research works using IGABEM for crack propagation analysis, this is the first application of the latter. In addition, the Schollmann criterion includes the influence of mode III behaviour on the propagation angle. As such, this study proposes a novel strategy for the determination of the updated crack front, allowing for the NURBS curve weights to adjust during the crack growth. Also, this study deals with a multi-patch modelling of the crack surfaces, which involves a fine-tuning algorithm for guaranteeing the required continuity between independent surfaces. Furthermore, the fatigue life assessment considers a linear interpolation of the SIFs in the Paris-Erdogan Law, permitting the use of larger crack increment lengths. By comparison with a reference solution from the literature, it is shown that the use of this linear interpolation does not introduce significant errors in the solution.

The numerical applications have demonstrated that the formulation obtains accurate values for the SIFs during the whole crack growth process. This is particularly advantageous because the exponential behaviour contained in the Paris-Erdogan Law results in the accumulation of errors if a high level of accuracy in SIFs is not maintained. The SIF accuracy is evidenced by agreement between the numerical results obtained and reference solutions for a variety of relevant problems. The crack growth criteria comparison shows that the Schollmann criterion and the hoop stress criterion yield similar results for the key engineering parameters describing the crack growth. This demonstrates that the incorporation of the Mode III behaviour in the equivalent SIF is sufficient to capture its effects during mixed-mode crack growth. In addition, the third application presents the capacity of the XIGABEM in addressing the fatigue crack growth phenomenon in a real-life complex engineering application.

The strategies proposed by this study can be extended to various other problems in three-dimensional fracture mechanics. Within fatigue analysis, the XIGABEM can be further adjusted for cases in which the cyclic load has an overload effect, which impacts the overall response by extending the required number of cycles until failure. In addition, the modelling of quasi-brittle fracture propagation using the IGABEM and the new scheme for the crack front update is also a possibility. Another future work is the combination of the proposed strategies in this study with the other enrichment strategies within XIGABEM for general cases in which the crack crosses the external boundary.

Acknowledgements

Sponsorship of this research project by the grants no 2019/18795-6 and 2022/00714-2 by the São Paulo Research Foundation (FAPESP) is greatly appreciated.

Appendix A. Geometrical data of elliptical crack

This appendix provides the geometrical data associated to the modelling of the coarse mesh of the section 5.1. APPENDIX A provides the control points coordinates and weights. Patches 1 to 6 have $p = q = 1$, with their corresponding knot vector being $\Xi_1 = \Xi_2 = \{0,0,1,1\}$. All other patches have $p = q = 2$ and their knot vector are $\Xi_1 = \Xi_2 = \{0,0,0,1,1,1\}$. Table A.2 refers to the control point connectivity in each patch. The first 8 control points and the first 6 patches represent the prism.

Control point	x_1	x_2	x_3	w
1	-24.0000	-48.0000	16.0000	1.00000000
2	24.0000	-48.0000	16.0000	1.00000000
3	-24.0000	48.0000	16.0000	1.00000000
4	24.0000	48.0000	16.0000	1.00000000
5	24.0000	48.0000	-16.0000	1.00000000
6	24.0000	-48.0000	-16.0000	1.00000000
7	-24.0000	-48.0000	-16.0000	1.00000000
8	-24.0000	48.0000	-16.0000	1.00000000
9	0.0000	0.0000	1.6000	1.00000000
10	2.4000	0.0000	1.6000	0.70710678
11	2.4000	0.0000	0.0000	1.00000000
12	-2.4000	0.0000	1.6000	0.70710678
13	0.0000	0.0000	0.0000	0.41421356
14	2.4000	0.0000	-1.6000	0.70710678

Control point	x_1	x_2	x_3	w
15	-2.4000	0.0000	0.0000	1.00000000
16	-2.4000	0.0000	-1.6000	0.70710678
17	0.0000	0.0000	-1.6000	1.00000000
18	0.0000	0.0000	-1.8000	1.00000000
19	0.0000	0.0000	-2.0000	1.00000000
20	-2.7000	0.0000	-1.8000	0.70710678
21	-3.0000	0.0000	-2.0000	0.70710678
22	-2.7000	0.0000	0.0000	1.00000000
23	-3.0000	0.0000	0.0000	1.00000000
24	2.7000	0.0000	-1.8000	0.70710678
25	2.7000	0.0000	0.0000	1.00000000
26	3.0000	0.0000	-2.0000	0.70710678
27	3.0000	0.0000	0.0000	1.00000000
28	0.0000	0.0000	1.8000	1.00000000
29	-2.7000	0.0000	1.8000	0.70710678
30	0.0000	0.0000	2.0000	1.00000000
31	-3.0000	0.0000	2.0000	0.70710678
32	2.7000	0.0000	1.8000	0.70710678
33	3.0000	0.0000	2.0000	0.70710678
34	0.0000	0.0000	1.6000	1.00000000
35	-2.4000	0.0000	1.6000	0.70710678
36	-2.4000	0.0000	0.0000	1.00000000
37	2.4000	0.0000	1.6000	0.70710678
38	0.0000	0.0000	0.0000	0.41421356
39	-2.4000	0.0000	-1.6000	0.70710678
40	2.4000	0.0000	0.0000	1.00000000
41	2.4000	0.0000	-1.6000	0.70710678
42	0.0000	0.0000	-1.6000	1.00000000
43	0.0000	0.0000	1.8000	1.00000000
44	2.7000	0.0000	1.8000	0.70710678
45	2.7000	0.0000	0.0000	1.00000000
46	0.0000	0.0000	2.0000	1.00000000
47	3.0000	0.0000	2.0000	0.70710678
48	3.0000	0.0000	0.0000	1.00000000
49	-2.7000	0.0000	1.8000	0.70710678
50	-3.0000	0.0000	2.0000	0.70710678
51	-2.7000	0.0000	0.0000	1.00000000
52	-3.0000	0.0000	0.0000	1.00000000
53	0.0000	0.0000	-1.8000	1.00000000

Control point	x_1	x_2	x_3	w
54	0.0000	0.0000	-2.0000	1.00000000
55	2.7000	0.0000	-1.8000	0.70710678
56	3.0000	0.0000	-2.0000	0.70710678
57	-2.7000	0.0000	-1.8000	0.70710678
58	-3.0000	0.0000	-2.0000	0.70710678

Table A.1: Control points and weights for the coarse mesh of the elliptical crack modelling.

Patch	Control points									
1	1	2	3	4						
2	4	2	5	6						
3	1	3	7	8						
4	4	5	3	8						
5	1	7	2	6						
6	7	8	6	5						
7	9	10	11	12	13	14	15	16	17	
8	17	18	19	16	20	21	15	22	23	
9	17	14	11	18	24	25	19	26	27	
10	9	12	15	28	29	22	30	31	23	
11	9	28	30	10	32	33	11	25	27	
12	34	35	36	37	38	39	40	41	42	
13	34	37	40	43	44	45	46	47	48	
14	34	43	46	35	49	50	36	51	52	
15	42	53	54	41	55	56	40	45	48	
16	42	39	36	53	57	51	54	58	52	

Table A.2: Connectivity of the elliptical crack model.

References

- [1] X. Lin, R. Smith, Finite element modelling of fatigue crack growth of surface cracked plates: Part i: The numerical technique, *Engineering Fracture Mechanics* 63 (5) (1999) 503–522.
- [2] X. Lin, R. Smith, Finite element modelling of fatigue crack growth of surface cracked plates: Part iii: Stress intensity factor and fatigue crack growth life, *Engineering Fracture Mechanics* 63 (5) (1999) 541–556.

- [3] M. Schöllmann, M. Fulland, H. Richard, Development of a new software for adaptive crack growth simulations in 3d structures, *Engineering Fracture Mechanics* 70 (2) (2003) 249–268.
- [4] A. Ural, G. Heber, P. A. Wawrzynek, A. R. Ingraffea, D. G. Lewicki, J. B. Neto, Three-dimensional, parallel, finite element simulation of fatigue crack growth in a spiral bevel pinion gear, *Engineering Fracture Mechanics* 72 (8) (2005) 1148–1170.
- [5] G. Sarego, Q. V. Le, F. Bobaru, M. Zaccariotto, U. Galvanetto, Linearized state-based peridynamics for 2-d problems, *International Journal for Numerical Methods in Engineering* 108 (10) (2016) 1174–1197. doi:<https://doi.org/10.1002/nme.5250>.
- [6] Y. Hu, E. Madenci, Peridynamics for fatigue life and residual strength prediction of composite laminates, *Composite Structures* 160 (2017) 169 – 184. doi:[10.1016/j.compstruct.2016.10.010](https://doi.org/10.1016/j.compstruct.2016.10.010).
- [7] J. Jung, J. Seok, Mixed-mode fatigue crack growth analysis using peridynamic approach, *International Journal of Fatigue* 103 (2017) 591–603. doi:<https://doi.org/10.1016/j.ijfatigue.2017.06.008>.
- [8] C. T. Nguyen, S. Oterkus, E. Oterkus, An energy-based peridynamic model for fatigue cracking, *Engineering Fracture Mechanics* 241 (2021) 107373. doi:<https://doi.org/10.1016/j.engfracmech.2020.107373>.
- [9] Y.-S. Lo, M. J. Borden, K. Ravi-Chandar, C. M. Landis, A phase-field model for fatigue crack growth, *Journal of the Mechanics and Physics of Solids* 132 (2019) 103684. doi:<https://doi.org/10.1016/j.jmps.2019.103684>.
- [10] A. Mesgarnejad, A. Imanian, A. Karma, Phase-field models for fatigue crack growth, *Theoretical and Applied Fracture Mechanics* 103 (2019) 102282. doi:<https://doi.org/10.1016/j.tafmec.2019.102282>.
- [11] P. K. Kristensen, E. Martínez-Pañeda, Phase field fracture modelling using quasi-newton methods and a new adaptive step scheme, *Theoretical and Applied Fracture Mechanics* 107 (2020) 102446. doi:<https://doi.org/10.1016/j.tafmec.2019.102446>.
- [12] P. Carrara, M. Ambati, R. Alessi, L. De Lorenzis, A framework to model the fatigue behavior of brittle materials based on a variational phase-field approach, *Computer Methods in Applied Mechanics and Engineering* 361 (2020) 112731. doi:<https://doi.org/10.1016/j.cma.2019.112731>.

- [13] J. Ding, T. Yu, W. Fang, S. Natarajan, An adaptive phase field modeling of fatigue crack growth using variable-node elements and explicit cycle jump scheme, *Computer Methods in Applied Mechanics and Engineering* 429 (2024) 117200. doi:<https://doi.org/10.1016/j.cma.2024.117200>.
- [14] N. Sukumar, D. L. Chopp, B. Moran, Extended finite element method and fast marching method for three-dimensional fatigue crack propagation, *Engineering Fracture Mechanics* 70 (1) (2003) 29–48. doi:[https://doi.org/10.1016/S0013-7944\(02\)00032-2](https://doi.org/10.1016/S0013-7944(02)00032-2).
- [15] J. Shi, D. Chopp, J. Lua, N. Sukumar, T. Belytschko, Abaqus implementation of extended finite element method using a level set representation for three-dimensional fatigue crack growth and life predictions, *Engineering Fracture Mechanics* 77 (14) (2010) 2840–2863. doi:<https://doi.org/10.1016/j.engfracmech.2010.06.009>.
- [16] J. Rannou, N. Limodin, J. Réthoré, A. Gravouil, W. Ludwig, M.-C. Baïetto-Dubourg, J.-Y. Buffière, A. Combescure, F. Hild, S. Roux, Three dimensional experimental and numerical multiscale analysis of a fatigue crack, *Computer Methods in Applied Mechanics and Engineering* 199 (21) (2010) 1307–1325, *multiscale Models and Mathematical Aspects in Solid and Fluid Mechanics*. doi:<https://doi.org/10.1016/j.cma.2009.09.013>.
- [17] J. Pereira, C. A. Duarte, X. Jiao, Three-dimensional crack growth with hp-generalized finite element and face offsetting methods, *Computational Mechanics* 46 (2010) 431–453. doi:<https://doi.org/10.1007/s00466-010-0491-3>.
- [18] H. Pathak, A. Singh, I. V. Singh, Fatigue crack growth simulations of 3-d problems using xfem, *International Journal of Mechanical Sciences* 76 (2013) 112–131. doi:<https://doi.org/10.1016/j.ijmecsci.2013.09.001>.
- [19] J. Garzon, P. O’Hara, C. A. Duarte, W. G. Buttlar, Improvements of explicit crack surface representation and update within the generalized finite element method with application to three-dimensional crack coalescence, *International Journal for Numerical Methods in Engineering* 97 (4) (2014) 231–273. doi:<https://doi.org/10.1002/nme.4573>.
- [20] P. O’Hara, J. Hollkamp, C. Duarte, T. Eason, A two-scale generalized finite element method for fatigue crack propagation simulations utilizing a fixed, coarse hexahedral mesh, *Computational Mechanics* 57 (1) (2016) 55–74. doi:<https://doi.org/10.1007/s00466-015-1221-7>.

- [21] A. Bergara, J. Dorado, A. Martin-Meizoso, J. Martínez-Esnaola, Fatigue crack propagation in complex stress fields: Experiments and numerical simulations using the extended finite element method (xfem), *International Journal of Fatigue* 103 (2017) 112–121. doi:<https://doi.org/10.1016/j.ijfatigue.2017.05.026>.
- [22] T. Hughes, J. Cottrell, Y. Bazilevs, Isogeometric analysis: Cad, finite elements, nurbs, exact geometry and mesh refinement, *Computer Methods in Applied Mechanics and Engineering* 194 (39) (2005) 4135 – 4195. doi:<https://doi.org/10.1016/j.cma.2004.10.008>.
- [23] Y. Bazilevs, X. Deng, A. Korobenko, F. L. Di Scalea, M. Todd, S. Taylor, Isogeometric fatigue damage prediction in large-scale composite structures driven by dynamic sensor data, *Journal of Applied Mechanics, Transactions ASME* 82 (9), cited by: 100; All Open Access, Green Open Access (2015). doi:[10.1115/1.4030795](https://doi.org/10.1115/1.4030795).
- [24] G. Bhardwaj, I. Singh, B. Mishra, Stochastic fatigue crack growth simulation of interfacial crack in bi-layered fgms using xiga, *Computer Methods in Applied Mechanics and Engineering* 284 (2015) 186 – 229, cited by: 87. doi:[10.1016/j.cma.2014.08.015](https://doi.org/10.1016/j.cma.2014.08.015).
- [25] G. Bhardwaj, I. Singh, B. Mishra, Fatigue crack growth in functionally graded material using homogenized xiga, *Composite Structures* 134 (2015) 269 – 284, cited by: 39. doi:[10.1016/j.compstruct.2015.08.065](https://doi.org/10.1016/j.compstruct.2015.08.065).
- [26] G. Bhardwaj, S. Singh, I. Singh, B. Mishra, T. Rabczuk, Fatigue crack growth analysis of an interfacial crack in heterogeneous materials using homogenized xiga, *Theoretical and Applied Fracture Mechanics* 85 (2016) 294 – 319, cited by: 55. doi:[10.1016/j.tafmec.2016.04.004](https://doi.org/10.1016/j.tafmec.2016.04.004).
- [27] Z. Si, Hirshikesh, T. Yu, W. Fang, S. Natarajan, An adaptive multi-patch isogeometric phase-field model for fatigue fracture, *International Journal of Mechanical Sciences* 271, cited by: 2 (2024). doi:[10.1016/j.ijmecsci.2024.109146](https://doi.org/10.1016/j.ijmecsci.2024.109146).
- [28] M. Shoheib, Stress intensity factor and fatigue life evaluation for important points of semi-elliptical cracks in welded pipeline by bezier extraction based xiga and new correlation model, *Engineering Analysis with Boundary Elements* 155 (2023) 264 – 280, cited by: 0. doi:[10.1016/j.enganabound.2023.05.052](https://doi.org/10.1016/j.enganabound.2023.05.052).
- [29] A. Portela, M. Aliabadi, D. Rooke, Dual boundary element incremental-analysis of crack-propagation, *Computer & Structures* 46 (2) (1993) 237–247. doi:[10.1016/0045-7949\(93\)90189-K](https://doi.org/10.1016/0045-7949(93)90189-K).

- [30] H.-K. Hong, J.-T. Chen, Derivations of integral equations of elasticity, *Journal of Engineering Mechanics* 114 (6) (1988) 1028–1044. doi:[http://dx.doi.org/10.1061/\(ASCE\)0733-9399\(1988\)114:6\(1028\)](http://dx.doi.org/10.1061/(ASCE)0733-9399(1988)114:6(1028)).
- [31] Y. Mi, M. Aliabadi, 3-dimensional crack-growth simulation using bem, *Computers & Structures* 52 (5) (1994) 871–878. doi:[10.1016/0045-7949\(94\)90072-8](https://doi.org/10.1016/0045-7949(94)90072-8).
- [32] B. Carter, P. Wawrzynek, A. Ingraffea, Automated 3-d crack growth simulation, *International Journal for Numerical Methods in Engineering* 47 (1-3) (2000) 229–253. doi:[10.1002/\(SICI\)1097-0207\(20000110/30\)47:1/3<229::AID-NME769>3.3.CO;2-U](https://doi.org/10.1002/(SICI)1097-0207(20000110/30)47:1/3<229::AID-NME769>3.3.CO;2-U).
- [33] B. Yang, S. Mall, K. Ravi-Chandar, A cohesive zone model for fatigue crack growth in quasibrittle materials, *International Journal of Solids And Structures* 38 (22-23) (2001) 3927–3944. doi:[10.1016/S0020-7683\(00\)00253-5](https://doi.org/10.1016/S0020-7683(00)00253-5).
- [34] A. P. Cisilino, M. Aliabadi, Dual boundary element assessment of three-dimensional fatigue crack growth, *Engineering Analysis with Boundary Elements* 28 (9) (2004) 1157–1173. doi:<https://doi.org/10.1016/j.enganabound.2004.01.005>.
- [35] K. Kolk, G. Kuhn, The advanced simulation of fatigue crack growth in complex 3d structures, *Archive of Applied Mechanics* 76 (11) (2006) 699–709. doi:<https://doi.org/10.1007/s00419-006-0092-y>.
- [36] S. G. F. Cordeiro, E. D. Leonel, An improved computational framework based on the dual boundary element method for three-dimensional mixed-mode crack propagation analyses, *Advances in Engineering Software* 135 (2019) 102689.
- [37] R. Simpson, S. Bordas, J. Trevelyan, T. Rabczuk, A two-dimensional isogeometric boundary element method for elastostatic analysis, *Computer Methods in Applied Mechanics and Engineering* 209-212 (2012) 87–100. doi:[10.1016/j.cma.2011.08.008](https://doi.org/10.1016/j.cma.2011.08.008).
- [38] M. Scott, R. Simpson, J. Evans, S. Lipton, S. Bordas, T. Hughes, T. Sederberg, Isogeometric boundary element analysis using unstructured t-splines, *Computer Methods in Applied Mechanics and Engineering* 254 (2013) 197–221. doi:<https://doi.org/10.1016/j.cma.2012.11.001>.
- [39] Y. Wang, D. Benson, Multi-patch nonsingular isogeometric boundary element analysis in 3d, *Computer Methods in Applied Mechanics and Engineering* 293 (2015) 71–91. doi:<http://dx.doi.org/10.1016/j.cma.2015.03.016>.

- [40] X. Peng, E. Atroshchenko, P. Kerfriden, S. P. A. Bordas, Isogeometric boundary element methods for three dimensional static fracture and fatigue crack growth, *Computer Methods in Applied Mechanics and Engineering* 316 (2017) 151–185. doi:<http://dx.doi.org/10.1016/j.cma.2016.05.038>.
- [41] F. Sun, C. Dong, Three-dimensional crack propagation and inclusion-crack interaction based on igabem, *Engineering Analysis with Boundary Elements* 131 (2021) 1–14. doi:<https://doi.org/10.1016/j.enganabound.2021.06.007>.
- [42] R. Simpson, J. Trevelyan, A partition of unity enriched dual boundary element method for accurate computations in fracture mechanics, *Computer Methods in Applied Mechanics and Engineering* 200 (1-4) (2011) 1–10. doi:<http://dx.doi.org/10.1016/j.cma.2010.06.015>.
- [43] R. Simpson, J. Trevelyan, Evaluation of j_1 and j_2 integrals for curved cracks using an enriched boundary element method, *Engineering Fracture Mechanics* 78 (4) (2011) 623–637. doi:<http://dx.doi.org/10.1016/j.engfracmech.2010.12.006>.
- [44] I. Alatawi, J. Trevelyan, A direct evaluation of stress intensity factors using the extended dual boundary element method, *Engineering Analysis with Boundary Elements* 52 (2015) 56–63. doi:<http://dx.doi.org/10.1016/j.enganabound.2014.11.022>.
- [45] G. Hattori, I. A. Alatawi, J. Trevelyan, An extended boundary element method formulation for the direct calculation of the stress intensity factors in fully anisotropic materials, *International Journal for Numerical Methods in Engineering* 109 (7) (2017) 965–981. doi:<http://dx.doi.org/10.1002/nme.5311>.
- [46] H. C. Andrade, J. Trevelyan, E. D. Leonel, A nurbs-discontinuous and enriched isogeometric boundary element formulation for two-dimensional fatigue crack growth, *Engineering Analysis with Boundary Elements* 134 (2022) 259–281. doi:[10.1016/j.enganabound.2021.09.019](https://doi.org/10.1016/j.enganabound.2021.09.019).
- [47] M. Rocha, J. Trevelyan, E. D. Leonel, An extended isogeometric boundary element formulation for three-dimensional linear elastic fracture mechanics, *Computer Methods in Applied Mechanics and Engineering* 423 (2024) 116872. doi:<https://doi.org/10.1016/j.cma.2024.116872>.
- [48] A. Portela, M. Aliabadi, D. Rooke, The dual boundary element method: effective implementation for crack problems, *International journal for numerical methods in engineering* 33 (6) (1992) 1269–1287. doi:<http://dx.doi.org/10.1002/nme.1620330611>.

- [49] G. Beer, B. Marussig, C. Duenser, The isogeometric boundary element method, Springer, 2020.
- [50] M. G. Cox, The Numerical Evaluation of B-Splines*, IMA Journal of Applied Mathematics 10 (2) (1972) 134–149. doi:10.1093/imamat/10.2.134.
- [51] C. De Boor, On calculating with b-splines, Journal of Approximation Theory 6 (1) (1972) 50 – 62. doi:https://doi.org/10.1016/0021-9045(72)90080-9.
- [52] C. De Boor, A practical guide to splines, Vol. 27, Springer-Verlag New York, 1978. doi:https://doi.org/10.1007/978-1-4612-6333-3.
- [53] L. Piegl, W. Tiller, The NURBS book, Springer Science & Business Media, 1996. doi:https://doi.org/10.1007/978-3-642-59223-2.
- [54] M. Guiggiani, A. Gigante, A General Algorithm for Multidimensional Cauchy Principal Value Integrals in the Boundary Element Method, Journal of Applied Mechanics 57 (4) (1990) 906–915. doi:10.1115/1.2897660.
- [55] M. Guiggiani, G. Krishnasamy, T. J. Rudolphi, F. J. Rizzo, A General Algorithm for the Numerical Solution of Hypersingular Boundary Integral Equations, Journal of Applied Mechanics 59 (3) (1992) 604–614. doi:10.1115/1.2893766.
- [56] S. G. F. Cordeiro, E. D. Leonel, Mechanical modelling of three-dimensional cracked structural components using the isogeometric dual boundary element method, Applied Mathematical Modelling 63 (2018) 415–444. doi:http://dx.doi.org/10.1016/j.apm.2018.06.042.
- [57] T. Greville, Numerical procedures for interpolation by spline functions, Journal of the Society for Industrial and Applied Mathematics, Series B: Numerical Analysis 1 (1) (1964) 53–68. doi:https://doi.org/10.1137/0701005.
- [58] J. T. Oden, C. A. Duarte, Solution of singular problems using hp clouds, Mathematics of Finite Elements and Applications 9 (1996) 35–54.
- [59] C. Duarte, I. Babuška, J. Oden, Generalized finite element methods for three-dimensional structural mechanics problems, Computers & Structures 77 (2) (2000) 215–232. doi:10.1016/s0045-7949(99)00211-4.
- [60] F. Frenet, Sur les courbes à double courbure, Journal de Mathématiques Pures et Appliquées 17 (1852) 437–447.

- [61] J.-A. Serret, Sur quelques formules relatives à la théorie des courbes à double courbure, *Journal de Mathématiques Pures et Appliquées* 16 (1851) 193–207.
- [62] F. Erdogan, G. C. Sih, On the Crack Extension in Plates Under Plane Loading and Transverse Shear, *Journal of Basic Engineering* 85 (4) (1963) 519–525. doi:10.1115/1.3656897.
- [63] M. Schöllmann, H. A. Richard, G. Kullmer, M. Fulland, A new criterion for the prediction of crack development in multiaxially loaded structures, *International Journal of Fracture* 117 (2002) 129–141.
- [64] H. d. C. e Andrade, E. D. Leonel, The multiple fatigue crack propagation modelling in nonhomogeneous structures using the dbem, *Engineering Analysis with Boundary Elements* 98 (2019) 296–309.
- [65] F. Sun, C. Dong, Effective elastic properties of three-dimensional multiple crack problems with the isogeometric boundary element parallel fast direct solver, *Engineering Analysis with Boundary Elements* 155 (2023) 1104–1122. doi:http://dx.doi.org/10.1016/j.enganabound.2023.07.038.
- [66] W. H. Gerstle, Finite and boundary element modelling of crack propagation in two and three dimensions using interactive computer graphics, Phd thesis, Cornell University, New York (1986).
- [67] R. LaGreca, M. Daniel, A. Bac, Local deformation of nurbs curves, *Mathematical methods for curves and surfaces*, Tromso (2004) 243.
- [68] N. Carlson, Nurbs surface fitting with gauss-newton, Master’s thesis, Luleå University of Technology (2009).
- [69] P. Ilie, A. Ince, Three-dimensional fatigue crack growth simulation and fatigue life assessment based on finite element analysis, *Fatigue & Fracture of Engineering Materials & Structures* 45 (11) (2022) 3251–3266.
- [70] H. Tada, P. Paris, G. Irwin, *The analysis of cracks handbook*, New York: ASME Press 2 (2000) 1.
- [71] K. Kishore, V. S. Gujre, S. Choudhary, A. S. Gujre, M. Vishwakarma, T. Thirumurgan, M. Choudhury, M. Adhikary, A. Kumar, Failure analysis of a 24 t crane hook using multi-disciplinary approach, *Engineering Failure Analysis* 115 (2020) 104666. doi:https://doi.org/10.1016/j.engfailanal.2020.104666.



Citation on deposit: Rocha, M., Trevelyan, J., & Leonel, E. D. (in press). Fatigue growth modelling of three-dimensional cracks with the Extended Isogeometric Boundary Element Method.

Engineering Analysis with Boundary Elements

For final citation and metadata, visit Durham

Research Online URL: <https://durham-repository.worktribe.com/output/3790471>

Copyright statement: This accepted manuscript is licensed under the Creative Commons Attribution 4.0 licence.

<https://creativecommons.org/licenses/by/4.0/>